THE ASTROPHYSICAL JOURNAL, 361:440–458, 1990 October 1

X-RAY SPECTRAL VARIABILITY AND COMPLEX ABSORPTION IN THE SEYFERT 1 GALAXIES NGC 4051 AND MCG −6-30-15

M. MATSUOKA, L. PIRO,[1] AND M. YAMAUCHI[2]
Institute of Physical and Chemical Research, Wako

AND

T. MURAKAMI
Institute of Space and Astronautical Science, Sagamihara
Received 1989 January 25; accepted 1990 March 28

ABSTRACT

GINGA observations of the Seyfert 1 galaxies NGC 4051 and MCG −6-30-15 have led to new and exciting results. (1) Large-amplitude (>50%) variations have been detected, down to time scales of 200 s, that confirm and extend previous *EXOSAT* results. (2) These intensity variations are associated with spectral changes, the spectrum being steeper when the source is brighter. Spectral variability is well described by spectral index changes that correlates closely with the 2–10 keV luminosity, increasing by $\sim\Delta\alpha \approx 0.4$–$0.5$ and centered on $\alpha \approx 1.7$ (photon index) when the flux increases by a factor of 3–4. (3) A flat spectral component has been detected in the spectrum of MCG −6-30-15 above 10 keV. This component is probably produced by absorption and Compton scattering of the central continuum by very thick ($N_H > 10^{24}$ cm^{-2}) cold matter in the environment of the central source. The detection of an iron fluorescence line at 6.4 keV with an equivalent width of ~200 eV supports this interpretation.

Subject headings: galaxies: individual (MCG −6-30-15, NGC 4051) — galaxies: Seyfert — galaxies: X-rays

I. INTRODUCTION

The first good-quality spectral survey of active galactic nuclei (AGNs; hereafter we refer to AGNs not including BL Lac objects) in the range 2–30 keV by *HEAO 1* A-2 (Mushotzky 1982, 1984*a*) showed a remarkable similarity of the spectra of these objects, well fitted by a power law with spectral index clustering closely around the "canonical" value $\alpha = 1.7$ (hereafter α is the photon index) whereas the corresponding X-ray luminosities were spread over about four orders of magnitude. The absorption present in some of these spectra was well reproduced by a uniform cold absorber model.

With the increasing sensitivity and wider energy band of X-ray instruments, this view has rather changed. In some objects the simple absorber model is no longer adequate, data requiring departures from uniformity (e.g., Holt *et al.* 1980; Reichert *et al.* 1985) or neutrality (e.g., Halpern 1984).

The picture of a "universal" or "canonical" spectrum has been also modified. There are many objects that show a spectral index significantly different from the "canonical" value (e.g., Lightman and Zdziarski 1987; Wilkes and Elvis 1987), but yet within a rather small interval of $\alpha \simeq 1.4$–2.0. Some AGNs show evidence of spectral variability. In all these objects (3C120, Halpern 1985; NGC 4151, Perola *et al.* 1986; NGC 7314, Turner 1987; NGC 5548, Branduardi-Raymont 1986) spectral variations are well described by spectral index changes that are correlated with the luminosity, the spectrum being steeper when the luminosity is higher. Typically a variation of $\Delta\alpha \simeq 0.3$–0.4, still confined within the interval $\alpha \simeq 1.4$–2.0, is associated with an intensity change of a factor of 3–4.

The LAC detector (Large Area proportional Counters) abroad *GINGA* (Makino 1987; Turner *et al.* 1989) with its large area and low background is a powerful instrument for studying such spectral changes. The Seyfert 1 galaxies NGC 4051 and MCG −6-30-15, whose *GINGA* observations are presented in this paper, were characterized by large-amplitude variations in the X-ray range, down to time scales of hours or less (NGC 4051: Lawrence *et al.* 1985, 1987; MCG −6-30-15: Pounds, Turner, and Warwick 1986; Pounds and Turner 1986). Moreover, in a previous *EXOSAT* observation of NGC 4051 (Lawrence *et al.* 1985) there was an indication of spectral variability, the spectrum being steeper when the source was brighter. These objects are therefore good targets for a spectral variability search during a typical *GINGA* observation (1–2 days). The results of these observations are presented and discussed here.

The absorbing matter, whose effect has been detected in the X-ray spectra of AGNs so far, is usually associated with the broad-line region (BLR) clouds (Mushotzky 1984*b*). On the other hand, in the last few years, an increasing evidence for the existence of matter nearby the central "engine," possibly in the form of an accretion disk, has risen, with the observation of the "big bump" (Malkan and Sargent 1982; Malkan 1983) and soft X-ray excesses (e.g., Arnaud *et al.* 1985). Recently, several authors have discussed the effect of such a matter on the X-ray spectra, pointing out the presence of spectral signatures in the X-ray band (Guilbert and Rees 1988; Lightman and White 1988). In this work we present high-quality X-ray spectra obtained by *GINGA* observations of MCG −6-30-15 and NGC 4051 and discuss how they can constrain the state of the matter in the environment of the central "engine."

In § II we describe observations and data reduction procedures. In §§ III and IV we present the results on temporal behavior, X-ray spectrum and spectral variability for MCG −6-30-15 and NGC 4051, respectively. In § V we discuss these results and present our conclusions.

[1] On leave from Istituto TE.S.R.E., C.N.R., Bologna. Now at I.A.S., C.N.R., Frascati, Italy.
[2] Also Osaka City University.

II. *GINGA* OBSERVATIONS AND DATA REDUCTION

The LAC instrument aboard *GINGA* satellite consists of eight proportional counters with a total area of 4000 cm^2 and an energy resolution of 18% (FWHM) at 6 keV (Turner *et al.* 1989). Observations with this instrument were performed from 1987 June 3 to 6 for NGC 4051 and from September 9 to 11 for MCG −6-30-15. Data on September 9 until 17:45 UT were collected with a low collimator efficiency (<0.3) and are not included in this analysis. MPC1 mode was used, which provides both detector identification and full spectral resolution in 48 pulse height channels with a 16 s time resolution. Background observations were performed for 1 day adjacent to the observations of the sources, pointing a "blank" sky nearby the two targets.

Since both sources were variable, with a 2–20 keV count rate from 10% to 100% of background, a careful and conservative data qualification and background subtraction were carried out. Data with a low geomagnetic cutoff rigidity (<10 GeV/c) or with a SUD count rate (surplus over upper discriminator = count rate above 37 keV) greater than 7.5 counts s^{-1} per detector, that correspond to high background regions, were excluded from analysis, as well as data corresponding to instrumental spikes and flares. Moreover, in the analysis of MCG −6-30-15 data, we did not use two external detectors, illuminated by the Sun with a β angle of $\sim 75°$. The other detectors were in the shadow of a solar panel. To improve the signal-to-noise ratio we used only top-layer data, because excess fluxes above the background level were found mainly in the 2–10 keV range, where the mid-layer has a low effective area but a background comparable to that of the top-layer.

Background was evaluated by using two independent methods, described in Turner *et al.* (1989) and in Hayashida *et al.* (1989). The background collected when the satellite is in the same position in the orbit, which repeats with a 1 day period, is approximately the same on 2 or 3 following days. Therefore we divide data of source and adjacent background in 15 parts per day, each one corresponding to one orbit of the satellite. Furthermore, data of each orbit were divided in narrow ranges of SUD values, because the SUD count rate is proportional to the background level. Background subtraction was finally carried out by using on source and background data in the same orbital position and with the same SUD distribution. When no background with the same orbit was available, we used a background of a nearby orbit for producing light curves, whereas we excluded those data from spectral analysis. This situation occurred for five "contact" orbits of MCG −6-30-15, when the satellite is activated by particles in passing through the South Atlantic Anomaly region. For spectral analysis, spectra from individual orbits were selected for having a reasonable statistic (integral counts in 2–20 keV range greater than ~ 1500 counts) and for being not strongly influenced by systematic effects in background subtraction (see following discussion), i.e., count rate greater than 3 counts s^{-1} (hereafter count rate refers to 2–20 keV range). For these reasons, six spectra of NGC 4051 were not considered in spectral analysis.

A similar but simpler method of background subtraction has been already applied to other Seyfert galaxies, giving reliable spectra both for bright (NGC 4151, Warwick *et al.* 1989b) and faint (Mrk 348, Warwick *et al.* 1989*a*) objects. In these cases the orbital dependence of background was not taken into account, but the authors just restricted the analysis to long periods when this effect is low, corresponding to orbits that do not pass through the South Atlantic Anomaly ("remote" orbits). Background and source data were then normalized using only the average SUD level.

The quality of the present procedure for data qualification and background subtraction is further supported by the quality of spectra obtained from the "contact" orbits, where the background is higher and more dependent on orbital position. These spectra give similar χ^2_ν and best-fit parameters as the remote orbits with the same flux level when fitted with the same model.

A final test was obtained by applying an independent method of background subtraction, as described in Hayashida *et al.* (1989). In this method, background is linearly related to a set of housekeeping and environmental parameters whose coefficients are evaluated by fitting the model to a set of "blank" sky observations. This method does not use a background measured nearby the source observation. We did not find any significant difference in the results obtained by using this and the previous method. In particular, best-fit parameters of summed spectra presented in § III*b* and IV*b* were consistent with those obtained by the first method. However, we found that the spectra obtained by the method of Hayashida *et al.* were more noisy, possibly due to small changes in background behavior on very long time scales. For this reason we present the results obtained with the first method.

The similarity of results derived with the two methods suggests that systematic errors in background subtraction should be less than statistical errors. Generally, two kinds of systematic errors could influence data, namely, residual uncertainties in calibrations and background subtraction. An estimation of the first effect is derived from the fit to the Crab spectrum with a power law with uniform absorption (Turner *et al.* 1989). Best-fit parameters are in agreement with previous measurements, but the value of $\chi^2_\nu = 2.6$ ($\nu = 37$) indicate the presence of fluctuations greater than statistical errors. Since the source count rate (~ 10000 counts s^{-1}) is much greater than the background level (~ 40 counts s^{-1}), any systematic effect in background subtraction is completely negligible. The source of this systematic error is thus attributed to residual uncertainties in calibrations, corresponding to 0.5% of the count rate per channel. A $\chi^2_\nu = 0.8$ ($\nu = 37$) obtains when this value is added (quadratically) to the statistical errors.

Systematic errors in background subtraction can be further divided in two parts: reproducibility of the internal (particle-induced) instrumental background and spatial fluctuations of the X-ray background (XRB). The level of XRB depends on the position in the sky, with a r.m.s. of ~ 0.8 counts s^{-1} in the 2–10 keV range (Hayashida *et al.* 1989). On the other hand, the photon spectrum of XRB fluctuation has a well-defined featureless shape, independent on the position (at high galactic latitude as for the present objects), and similar to the spectrum of Seyfert galaxies. We conclude that XRB fluctuations will neither influence the spectral shape nor increase the variance of the spectra of the present objects (or any object with a similar spectral shape), but only increase the uncertainty in the absolute flux of the source of 0.8 counts s^{-1}.

Even though residual uncertainties in the reproducibility of internal background produce fluctuations lower than those of XRB, they should affect more severely the variance of source spectra, because their pulse height spectrum is more randomly distributed. The r.m.s. value of these fluctuations has been

evaluated by Hayashida *et al.* (1989), corresponding to 3×10^{-2} counts s^{-1} keV^{-1} below 10 keV and rapidly decreasing below 10^{-2} counts s^{-1} keV^{-1} at higher energies. These values are much lower than statistical errors of spectra of single orbits presented in §§ III*c* and IV*c*, and correspond to 30%–60% of statistical errors of summed spectra presented in §§ III*b* and IV*b*. Given the uncertainty in the contribution of these fluctuations to the variance of the source spectra, we included in our data only the systematic error in calibrations. However, we evaluated that the contribution of fluctuations of the instrumental background can at most reduce χ^2_ν values of 10%–30%, with no significant effect on the value of best-fit parameters. The maximum reduction would obtain for the low and mid level spectra of MCG −6-30-15 (§ III*b*) and for the mid-low and mid-high level spectra of NGC 4051 (§ IV*b*).

III. MCG −6-30-15

a) Light Curve

The light curve of MCG −6-30-15 in the energy range 1.2–22 keV is shown in Figure 1*a*, top panel, with a time bin of 128 s. Empty regions correspond to Earth occultation or high background zones. The total live time is ~25,000 s. The source count rate is highly variable, up to a factor of 3 on a time scale of hours of less, and the light curve is characterized by amplitude variations on all the time scales detectable by the instrument. This behavior is similar to that observed by the ME instrument aboard *EXOSAT* (Pounds, Turner, and Warwick, *et al.* 1986), but the larger area and lower background of LAC allow the detection of variability on shorter time scales. In Figure 1, bottom panel, we show, as an example, the enlargement of data indicated by the arrow (*b*) in Figure 1, top panel. Variations of 50% or more are clearly seen with a time scale of ~3–5 minutes.

The typical temporal structure of data stream, 10–20 minutes of data followed by an empty region of 80–90 minutes, which repeats with a periodicity of 100 minutes, and the small ratio of the effective/observing time (~20%), introduce heavily spurious effects (particularly the windowing effect; Deeming 1975) in a power spectrum obtained from the entire light curve. Nevertheless, a power spectral analysis is possible on shorter times scales, by limiting the analysis to the short continuous data segments of single orbits. We selected 11 data sets with a minimum uninterrupted coverage of 1000 s. Data were binned with a 16 s time bin. The corresponding power spectra were summed to produce the average spectrum shown in Figure 2. Source power above noise level is present up to $\sim 4 \times 10^{-3}$ Hz, as already noted from a visual inspection of Figure 1, bottom panel.

b) X-Ray Spectrum

Spectra from 17 orbits were obtained by using the procedure and selection criteria described in § II. As shown in the following, the spectral shape depends on the intensity of the source, the spectrum being steeper when the intensity is higher. To avoid the introduction of spurious features that could be created by adding spectra with different shapes, we summed the spectra of single orbits in three ranges of intensity (low, middle, and high). The corresponding statistical errors were computed taking into account that some spectra (those with the same orbit) were obtained by using the same background. The average count rate and selected interval, integration time and incident flux of each spectrum are given in Table 1. This table also gives the background exposure times and the mean background count rate.

Several models were fitted to these spectra in the 2–37 keV range. A simple power-law model with uniform cold absorp-

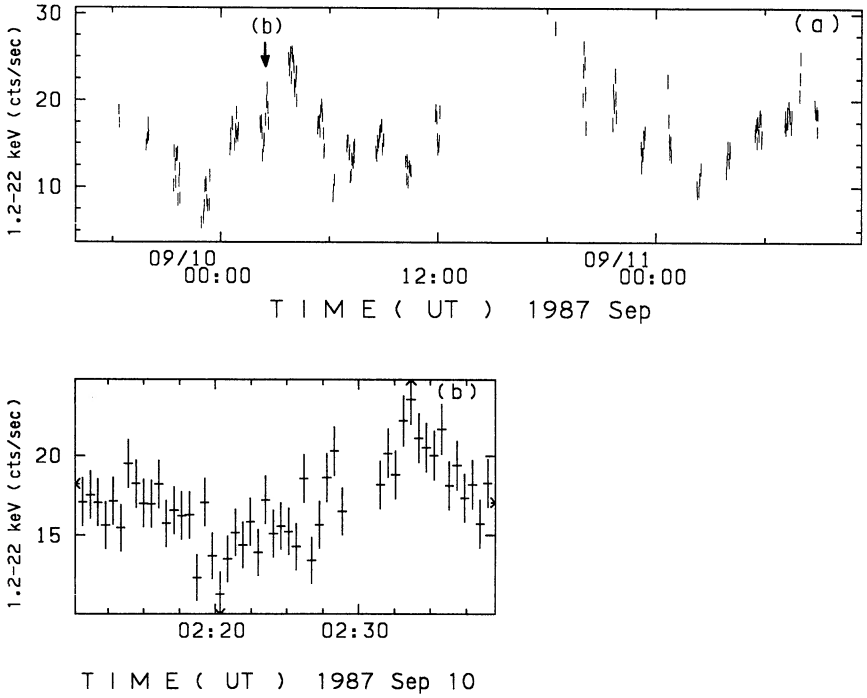

FIG. 1.—Light curve of MCG −6-30-15 in the energy band 1.2–22 keV summed on six detectors. *Top panel*: Overall light curve, with a time bin of 128 s. *Bottom panel*: Expanded light curve of data of the orbit corresponding to "(*b*)" in top panel with a time bin of 32 s.

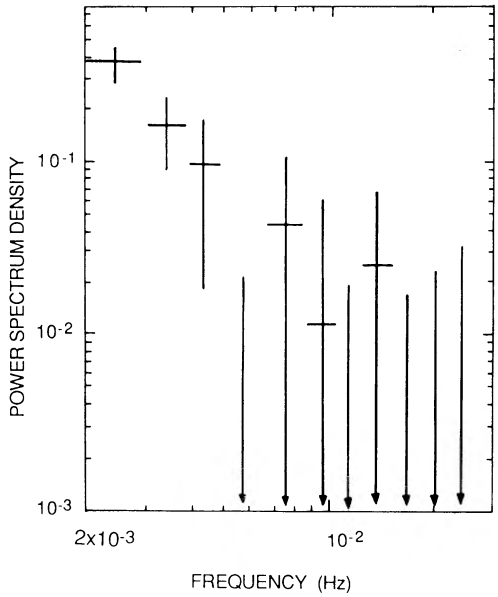

FIG. 2.—Power spectrum of MCG −6-30-15 in the same energy range as Fig. 1. Poissonian noise power is subtracted in this figure.

tion and solar abundances (cross sections from Morrison and McCammon 1983) gives unsatisfactory results: the reduced χ^2 for the high-, middle-, low-intensity spectra are, respectively, $\chi^2_\nu = 2.7$, 3.5, 1.5, with $\nu = 20$. In Figure 3*a* the pulse height spectrum and the best-fit power law of the middle intensity spectrum are plotted. Inspection of residuals shows an emission line around 6.4 keV, an enhanced deficit of counts between 7 and 15 keV and positive residuals at higher energies. Similar features are present in the other spectra. The fitting procedure was therefore repeated introducing in the model a narrow line (free parameters: energy and intensity) and an edge (free parameters: energy and absorption column density). The total number of free parameters was 7. The best-fit mean positions of line and edge for the three spectra were (6.20 ± 0.15) keV and (7.2 ± 0.6) keV, respectively, in agreement with the fluorescence line and edge energies from neutral iron, corrected for the redshift of the galaxy (corresponding to 6.35 keV and 7.05 keV, respectively). Best-fit values of the other parameters are summarized in Table 2A. The average value of iron column density, expressed as $N_{\rm HFe} = N_{\rm Fe}\,10^{4.48}$, is $N_{\rm HFe} = (3.8^{+1.4}_{-1.2})$ 10^{22} cm^{-2} (hereafter errors and upper limits are at a 90% confidence level), whereas the low-energy absorption is consistent with zero, with an upper limit of 0.25×10^{22} cm^{-2}. The optical depth of the iron edge is actually more enhanced, being constrained in the previous fit by the iron L shell absorption that is equivalent to a low-energy column density of $\sim N_{\rm HFe}/10$. Neglecting the L shell absorption we obtained average values of $N_{\rm HFe} = (16.5^{+6.5}_{-2.5}) \times 10^{22}$ cm^{-2} and $N_{\rm H} = (0.25^{+0.38}_{-0.12}) \times 10^{22}$ cm^{-2}. These results would imply an iron abundance more than one order of magnitude greater than the solar value, never observed in other cosmic sources. More interestingly, they could be explained by a reduction of opacity of atoms lighter than iron, produced by photoionization of the hard central continuum (Krolik and Kallman 1984). But, as explained in more detail in the discussion, this possibility is ruled out by the inconsistency between the high-ionization state required to reproduce the opacity ratio at the iron edge and lower energies, and the energies of the iron line and iron edge, that indicate lowly ionized or cold matter.

Then we considered another modification to the uniform cold absorber, namely the partial covering or "leaky" absorber model, that could fit these spectra keeping the abundance to the cosmic value. This model is expressed by the formula:

$$F(E) = \{CE^{-\alpha}[1 + f_{\rm cov}/(1 - f_{\rm cov}) \exp(-\sigma(E)N_{\rm Hcov})] + I_{\rm Fe}\} \times \exp(-\sigma(E)N_{\rm H}) . \quad (1)$$

Free parameters of the model were the spectral index of the underlying continuum (α), the normalization of the uncovered component (C), the uncovered intensity of the iron line ($I_{\rm Fe}$), the fraction of the source ($f_{\rm cov}$) covered by a column density $N_{\rm Hcov}$, and an additional column density ($N_{\rm H}$) covering uniformly all these components. Hereafter the energy of the line is fixed at 6.35 keV. The results are presented in Table 2B. The improvement of χ^2_ν values compared to the previous model is significant at 95, 99, 99% confidence level for the low, middle, and high spectra, respectively. The new result, that stands out in Table 2B, is the very high column density, $N_{\rm Hcov} = (6^{+4}_{-2}) \times 10^{24}$ cm^{-2}, that covers ~60% of the source. Note that the power-law indexes derived for this model are systematically greater (steeper) than the indexes derived for the simple power-law model. In Figure 3*b* we present the pulse height spectrum of the middle intensity spectrum, along with the best-fit model and its separate components. The covered component becomes comparable to the uncovered one above 15 keV, producing a high-energy bump in the spectrum.

A more sophisticated partial covering model than the simple

TABLE 1

COUNT RATE, EFFECTIVE EXPOSURE TIME, AND INCIDENT FLUX OF THE SPECTRA OF MCG −6-30-15 SUMMED IN THREE INTENSITY LEVELS

	Source				
Level	Count Rate[a] (Count s^{-1}) Range	Mean	Exposure Time[b] (s)	F(2–10 keV)[c]	Background[d] Exposure Time (s)
Low	10–14	12.4	5713	3.7	7667
Mid	14–18	16.2	9464	4.8	9730
High	18–24	20.4	4559	6.1	6527

[a] Count rate in the 2–20 keV range summed on six detectors.
[b] The exposure time is not corrected for the collimator efficiency, corresponding to ~80%.
[c] The incident flux (10^{-11} ergs cm^{-2} s^{-1}) is independent from the model within 5%.
[d] Background level is similar for the three spectra and corresponds to ~34 counts s^{-1} for six detectors.

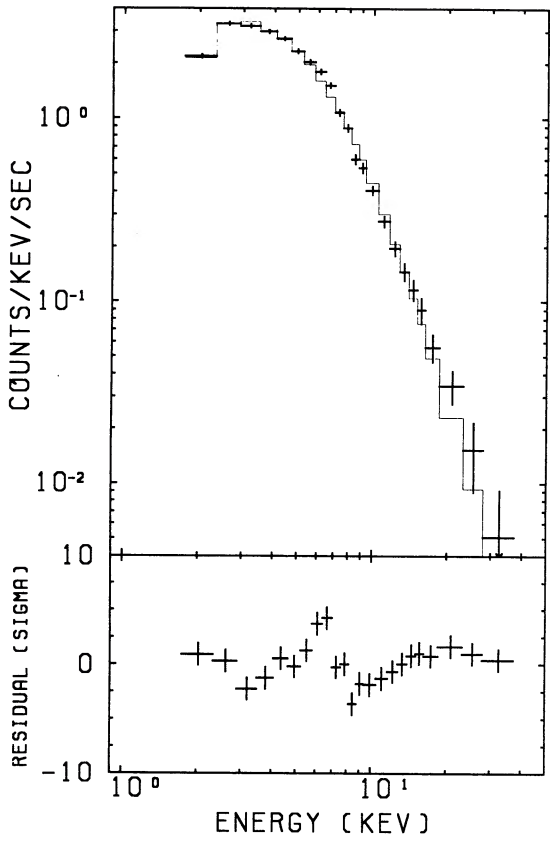

FIG. 3*a*

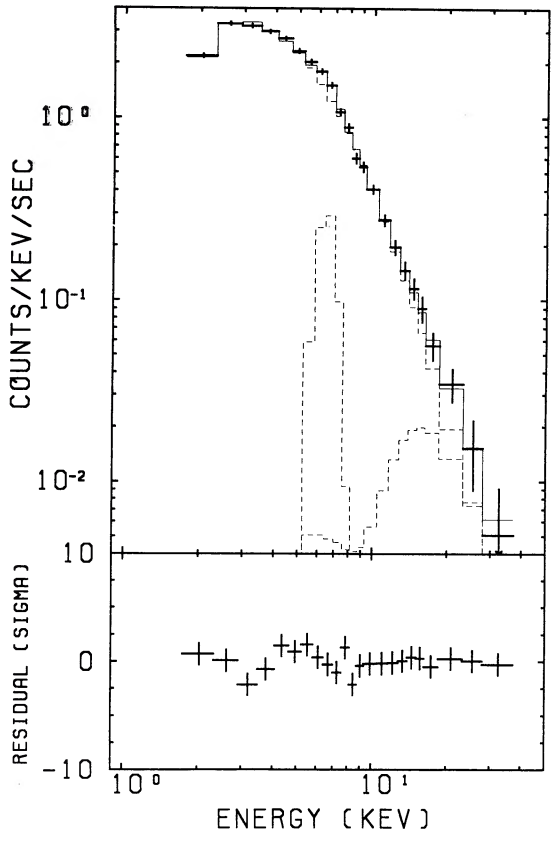

FIG. 3*b*

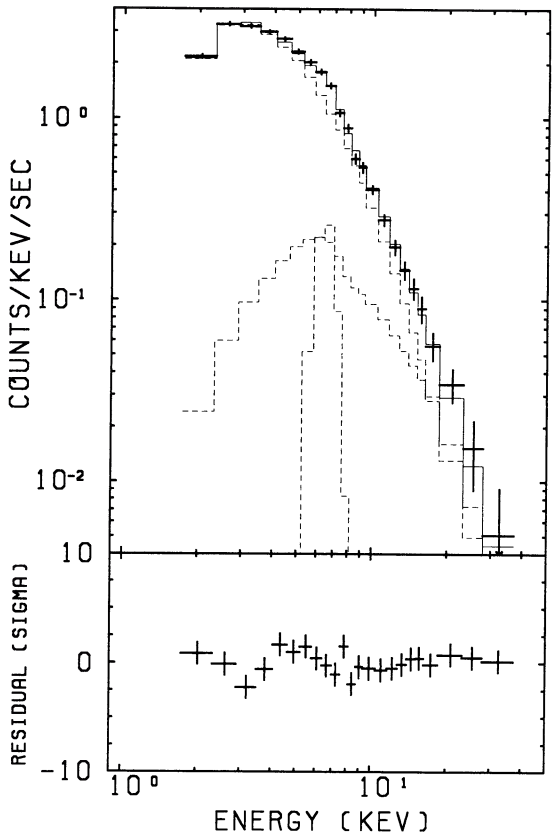

FIG. 3*c*

FIG. 3.—(*a*) Fit of a power law with uniform cold absorber to the middle intensity level spectrum of MCG −6-30-15. The result is not satisfactory ($\chi^2_\nu = 3.5$ with $\nu = 20$). Residuals are plotted in units of standard deviation. (*b*) Same as in (*a*) but with a fit with partial covering model with solar abundances and narrow emission line. The result is definitely better ($\chi^2_\nu = 1.1$ with $\nu = 17$). The emission components of the model are plotted with dashed lines. (*c*) Same as in (*a*) with a reflection model ($\chi^2_\nu = 1.2$ with $\nu = 18$).

one applied above is the Poissonian absorber model, that is more appropriate when the absorber is composed by clouds. In this case the fraction of the source covered by a number n of clouds is given by the Poisson distribution, whose mean value, μ, represents the mean number of clouds along the line of sight. The other parameter of this absorbing model is the column density of a single cloud, N_{HC}. The other free parameters were the same as those used in the simple partial covering model, with the exception of C, here representing the normalization of the underlying continuum. The results of the fit are presented in Table 2C, and can be directly compared with those of the partial covering model in Table 2B. Both models give an equivalent good description of the X-ray spectrum of MCG −6-30-15, and, in particular, of its absorbing matter. The column density of a single cloud $N_{HC} = (5^{+2}_{-1}) \times 10^{24}$ cm^{-2}, and the fraction of the source covered by one or more clouds, $1 - \exp(-\mu) = 0.63$, are also consistent with the values of column density and covering fraction of the previous model.

Then we applied the partial covering model with iron abundance as free parameter and using only the iron K edge photoelectric absorption. The reduced χ^2 for the low-, middle- and high-intensity spectra were, respectively, $\chi^2_\nu = 1.4, 1.0, 1.0$, with $\nu = 16$. All the spectra were consistent with a model in which 35% of the source is covered by matter with $N_{HFe} =$

TABLE 2

SPECTRAL FITS TO THE SPECTRA OF MCG −6-30-15

A. POWER LAW ($\nu = 16$)

Level	C[a]	α[b]	N_H[c]	N_{HFe}[d]	I_{Fe}[e]	χ^2_ν
Low	7.0 ± 0.8	1.50 ± 0.06	$0.0^{+0.4}_{0.0}$	$4.0^{+3.0}_{-2.0}$	1.13 ± 0.43	1.9
Mid	11.0 ± 0.9	1.63 ± 0.04	$0.0^{+0.3}_{0.0}$	$3.0^{+3.0}_{-2.0}$	1.43 ± 0.37	1.5
High	17.5 ± 1.6	1.76 ± 0.04	$0.0^{+0.6}_{0.0}$	$4.0^{+2.0}_{-1.5}$	0.60 ± 0.50	1.2
Mean	...	1.66 ± 0.02	$0.0^{+0.25}_{0.0}$	$3.8^{+1.4}_{-1.0}$	1.13 ± 0.25	...

B. POWER LAW WITH PARTIAL COVERING AND SOLAR ABUNDANCES ($\nu = 17$)

Level	C[a,f]	α[b]	N_H[c]	N_{Hcov}[c]	I_{Fe}[e,f]	f_{cov}	χ^2_ν
Low	8.1 ± 1.5	1.60 ± 0.10	$0.7^{+0.5}_{-0.3}$	600^{+800}_{-300}	1.26 ± 0.47	0.64 ± 0.24	1.6
Mid	$12.2 + 1.5$	1.70 ± 0.07	$0.5^{+0.3}_{-0.2}$	550^{+450}_{-250}	1.60 ± 0.40	0.60 ± 0.22	1.1
High	19.6 ± 2.4	1.84 ± 0.07	$0.6^{+0.4}_{-0.2}$	1000^{+2000}_{-800}	0.77 ± 0.53	0.70 ± 0.20	0.9
Mean	...	1.74 ± 0.04	$0.57^{+0.22}_{-0.13}$	600^{+400}_{-200}	1.29 ± 0.26	0.65 ± 0.13	...

C. POWER LAW WITH POISSONIAN ABSORBER ($\nu = 17$)

Level	C[a,g]	α[b]	N_H[c]	N_{HC}[c]	I_{Fe}[e,f]	μ	χ^2_ν
Low	24.3 ± 7.0	1.60 ± 0.10	$0.7^{+0.5}_{-0.3}$	500^{+350}_{-200}	1.26 ± 0.46	1.1 ± 0.3	1.6
Mid	34.7 ± 8.0	1.71 ± 0.07	$0.5^{+0.3}_{-0.2}$	500^{+250}_{-200}	1.60 ± 0.40	1.0 ± 0.2	1.1
High	51.3 ± 10.0	1.82 ± 0.07	0.6 ± 0.2	600^{+700}_{-300}	0.77 ± 0.50	1.0 ± 0.4	1.0
Mean	...	1.74 ± 0.04	$0.58^{+0.18}_{-0.13}$	500^{+200}_{-100}	1.29 ± 0.25	1.0 ± 0.15	...

D. REFLECTION MODEL ($\nu = 18$)

Level	C[a,f]	α[b]	N_H[c]	r[h]	I_{Fe}[e,f]	χ^2_ν
Low	10.1 ± 3.1	1.79 ± 0.12	$0.9^{+0.6}_{-0.4}$	2.3 ± 1.8	1.13 ± 0.43	1.7
Mid	15.7 ± 3.5	1.91 ± 0.08	0.8 ± 0.4	2.2 ± 1.6	1.43 ± 0.40	1.2
High	24.0 ± 5.3	2.01 ± 0.08	0.9 ± 0.4	2.0 ± 1.6	0.60 ± 0.50	1.1
Mean	...	1.93 ± 0.05	0.85 ± 0.25	2.2 ± 1.0	1.11 ± 0.25	...

E. TWO POWER LAWS ($\nu = 17$)

Level	C_1[a]	α_1[b]	N_H[c]	C_2[i]	α_2[b]	I_{Fe}[e]	χ^2_ν
Low	8.3 ± 2.0	1.61 ± 0.14	$0.7^{+0.4}_{-0.3}$	7^{+400}_{-7}	$-(1.1 \pm 1.2)$	1.30 ± 0.46	1.8
Mid	12.7 ± 2.5	1.73 ± 0.11	$0.5^{+0.3}_{-0.2}$	13^{+400}_{-13}	$-(1.0 \pm 1.0)$	1.63 ± 0.40	1.3
High	20.0 ± 3.5	1.85 ± 0.10	0.7 ± 0.3	$0.7^{+130}_{-0.7}$	$-(2.0^{+1.0}_{-1.4})$	0.83 ± 0.50	0.9
Mean	...	1.75 ± 0.07	0.61 ± 0.18	...	$-(1.32 \pm 0.65)$	1.31 ± 0.26	...

F. THERMAL BREMSSTRAHLUNG POWER LAW ($\nu = 17$)

Level	C_1[a]	κT[j]	N_H[c]	C_2[i]	α_2[b]	I_{Fe}[e]	χ^2_ν
Low	7.7 ± 2.1	18.8 ± 3.4	$0.6^{+0.4}_{-0.3}$	110^{+530}_{-110}	$-(0.5^{+0.9}_{-0.5})$	1.26 ± 0.43	1.8
Mid	10.8 ± 2.2	14.3 ± 2.8	$0.3^{+0.3}_{-0.2}$	220^{+430}_{-220}	$-(0.4^{+1.2}_{-0.3})$	1.56 ± 0.40	1.3
High	15.7 ± 3.4	11.6 ± 3.4	$0.4^{+0.3}_{-0.2}$	120^{+660}_{-120}	$-(0.6^{+1.6}_{-0.4})$	0.73 ± 0.50	0.9
Mean	..	14.8 ± 1.8	0.4 ± 0.2	...	$-(0.5^{+0.7}_{-0.2})$	1.31 ± 0.26	...

NOTES.—Range of fit 2–37 keV. Errors are 90% confidence level for one interesting parameter.

[a] Normalization in 10^{-3} photons cm^{-2} s^{-1} keV^{-1} at 1 keV.

[b] Photon index.

[c] Column density in 10^{22} cm^{-2}.

[d] $N_{HFe} = N_{Fe}\, 10^{4.48}$ in 10^{22} cm^{-2}. The iron cross section includes both the K and L shell absorption.

[e] Line intensity in 10^{-4} photons cm^{-2} s^{-1}.

[f] Normalization of the uncovered or direct component.

[g] Normalization of the underlying power law.

[h] Normalization of the reflected component relative to the direct component (eq. [2]).

[i] Normalization in 10^{-7} photons cm^{-2} s^{-1} keV^{-1} at 1 keV.

[j] Temperature in keV.

$(5^{+5}_{-3}) \times 10^{24}$ cm^{-2} and $N_{Hcov} = (3.0^{+1.5}_{-1.0}) \times 10^{23}$ cm^{-2}. We consider this model unsatisfactory for the following reasons: (1) The addition of one more parameter to the partial covering model with solar abundances does not yield a significant improvement of χ^2. (2) Such an iron overabundance, when explained by a photoionized matter, would imply a high-ionization state, with an iron edge around 8.5 keV. We repeated fits with iron edge energy as free parameter, obtaining a mean energy of (7.0 ± 0.3) keV. (3) The shape of the covered component below the iron edge is similar to a wide line centered around 6 keV. In fact, the intensity of the iron line obtained using this model is zero (we note that this particular

shape, where the iron line is reproduced by the covered component, provides a better constraint to the edge energy compared to the simple power-law model).

The possibility that the iron line is broad, suggested by the previous point, has been explored in more detail by fitting the partial covering model with solar abundances with the line width as free parameter. Reduced chi-squared values of 1.2, 1.0, 0.9, for the low-, middle-, and high-intensity spectra, respectively, are obtained, to be compared with the corresponding values of 1.6, 1.1, and 0.9 derived from the same model with a narrow line (Table 2B). Only for the low-intensity spectrum there is a significant improvement of χ^2 (98% confidence level derived by applying the F test) obtained with a width (σ) of (1.0 ± 0.5) keV. For the other spectra the value of the width is consistent with zero. Since the intensity of the line seems independent on the level of the continuum (Table 1 and discussion in § V*b*), larger deviations from a narrow line distribution would be expected when the continuum level is low, that could explain the detection of a broad line only for the low-intensity spectrum. On the other hand, systematic effects in background subtraction discussed in § II should be also larger for the low-intensity spectrum. Taking into account their maximum contribution to the errors, reduced χ^2 for the partial covering model with a narrow line would reduce to satisfactory values of 1.2, 0.9, and 0.8 for the low-, middle-, and high-level spectra, respectively.

The value of $N_{\rm Hcov}$ derived from the fit with the partial covering model is very high, and the effects of Compton scattering cannot be neglected. Due to multiple scattering, the path length of photons while traversing the medium is increased by a factor of about τ_T, the optical depth for Compton scattering (e.g., Rybicki and Lightman 1979). The true value of column density, $N_{\rm Htrue}$, will be then given by $N_{\rm Htrue} = N_{\rm Hcov}/\tau_T = (N_{\rm Hcov}/\sigma_T)^{1/2}$. For $N_{\rm Hcov} = 6 \times 10^{24}$ cm^{-2} it obtains $N_{\rm Htrue} = 3 \times 10^{24}$ cm^{-2}, $\tau_T = 2$. The scattering will not greatly modify the emergent spectrum, because the cross section is independent on the energy range in the LAC and the relative change of energy of a photon after traversing the medium is very small, being about $-nE/mc^2 \approx 0.1$, where $n \approx \tau_T^2$ is the number of scattering (Rybicki and Lightman 1979). Finally, $f_{\rm cov}$ should be considered as an upper limit, because of the additional contribution of photons scattered into our direction from matter lying outside our line of sight. The spectral shape of this reflected component is roughly similar to the covered component (Lightman and White 1988), because photons reflected into our direction will traverse an average optical depth of the order of τ_T, thus a column density of $\sim 1/\sigma_T = 2\ 10^{24}$ cm^{-2}. The relative weight of the reflected and covered component depends on the distribution of the matter around the central source. However, if the column density is greater than $\sim 10^{25}$ cm^{-2}, the covered component will be no longer visible in the LAC range, and the spectrum would reduce to the direct and a reflected component only.

We studied in more detail this case. The spectrum of the reflected (more correctly, reprocessed) component was computed by using the formulae given in Lightman and White (1988) and White, Lightman, and Zdziarski (1988), which take into account both Compton scattering and photoelectric absorption in a cold medium of solar abundances. Iron line emission, which is expected from fluorescence process following absorption of a photon by the K shell of iron, is not included in their formulae, and we add it as a free parameter to the model expressed by

$$F(E) = \{CE^{-\alpha}[1 + rA(E, \alpha)] + I_{\rm Fe}\} \exp(-\sigma N_{\rm H}), \quad (2)$$

where $CE^{-\alpha}$ represents the direct component, expressed as a simple power law, $CE^{-\alpha}rA(E, \alpha)$ is the reflected (reprocessed) component, $A(E, \alpha)$ is the corresponding X-ray albedo of the medium, and r is the ratio between the reflected and direct components. In the following we will refer to this model as the reflection model. It is worth noticing that the spectral shape of the reflected component depends only on the spectral index of the direct component and is independent of the column density of the thick, reflecting medium (Piro *et al.* 1990). Therefore, the total number of free parameters is 5, one less than the partial covering model. The results of the fit are presented in Table 2D. Reduced chi-squared values are similar to those obtained with the partial covering model. The overall spectral shape is again characterized by bump above 8 keV, produced by the increasing contribution of the reflected component (Fig. 3*c*). As in the case of the partial covering model, the spectral indexes are systematically greater than those derived for the simple power-law model.

So far we have shown as the X-ray spectrum of MCG −6-30-15 can be reproduced by taking into account the effects produced by matter with a very high column density on to an underlying continuum expressed by a simple power law. Now we examine the alternative case of a complex continuum emission and a simple uniform absorption with solar abundances. The continuum emission was described by a two-component model, namely, two power laws, and a power law with thermal bremsstrahlung. The results are presented in Table 2E and 2F. Values of chi square are slightly worse than those obtained by the partial covering and the reflection model. The thermal bremsstrahlung–power-law model was introduced to verify whether the complex spectral shape could be explained by the presence of a strong soft X-ray excess (represented by the thermal bremsstrahlung) on the top of the primary hard power-law emission. However, the best fit is obtained when the primary emission component is the thermal bremsstrahlung with a very high temperature ($\kappa T > 10$ keV), whereas the power law represents a hard tail which dominates the emission above 15 keV. Similar results are obtained for the two power-law model, where the crossing point between the primary steeper component ($\alpha \sim 1.6$–1.8) and the hard tail ($\alpha < 0$) is around 15 keV. Note that the error of the normalization of the hard power law is very large because this parameter is strongly correlated with the spectral index α_2. The flux of the hard power law is actually not consistent with zero, as appears from the significant improvement of χ^2 values compared to a fit with a single power law.

These results confirm that the major deviations from a simple model, such as a power law, are produced by a new flat component above 8–10 keV. This flat component may be only effectively flatter, as in the partial covering and reflection models, or it may be intrinsically flatter, as assumed in the thermal bremsstrahlung–power law and two power-law models. In these latter models, however, the slope of the power law is too flat ($\alpha < 0$) to be consistent with the spectral slope of Seyfert galaxies at higher energies (Rothschild *et al.* 1983). These models can be reconciled with the measurements at higher energies only if the new hard component recovers a steeper spectral index above about 30 keV, as in the partial covering and reflection models.

A last comment regards the "iron edge" feature detected in the fit with a simple power law. The spectral flattening around 8 keV (whether effective or intrinsic) will force the spectral index of the simple power law to a lower (flatter) value, thus producing negative residuals (data-model) in the 7–10 keV range, which simulate an unusually deep iron edge. As an "*a posteriori*" check, we have produced simulated spectra using the partial covering model with solar abundances and parameters as given in Table 2B and integration time as given in Table 1, and we have fitted these spectra with a simple power law with uniform absorption and iron edge energy and optical depth as free parameters. Best-fit parameters, including those of the iron edge, were consistent with those obtained performing a fit with the same model on the real data (Table 2A). The real iron edge present in the covered or reflected component with solar abundances, when diluted with the direct emission, would produce negligible (<0.5%) deviations in the case of the partial covering model, or would be rather small in the case of the reflection model ($N_{\rm HFe} \approx 4 \times 10^{22}$ cm^{-2} to be compared with a depth corresponding to 16.5×10^{22} cm^{-2}).

c) *Spectral Variability*

Another important and new result obtained from *GINGA* observations of MCG —6-30-15 is the detection of spectral variability. The spectral shape depends on the luminosity, the spectrum being steeper when the source is brighter. This is clearly shown in Figure 4, where we present the pulse height ratio between the high-intensity and low-intensity spectra. We note the following. (1) The reduced χ^2 for a constant hypothesis is $\chi^2_\nu = 5.5$ ($\nu = 22$), that confirms the high statistical significance of spectral variations. (2) The high-intensity spectrum is steeper (softer) than the low-intensity one. (3) Such spectral changes are not produced by a variation of the covered or reflected component. In fact, spectral variations are present well below 10 keV, where the contributions of these components is negligible (Fig. 3*c*). At the end of the section we present a direct test that confirms this indication.

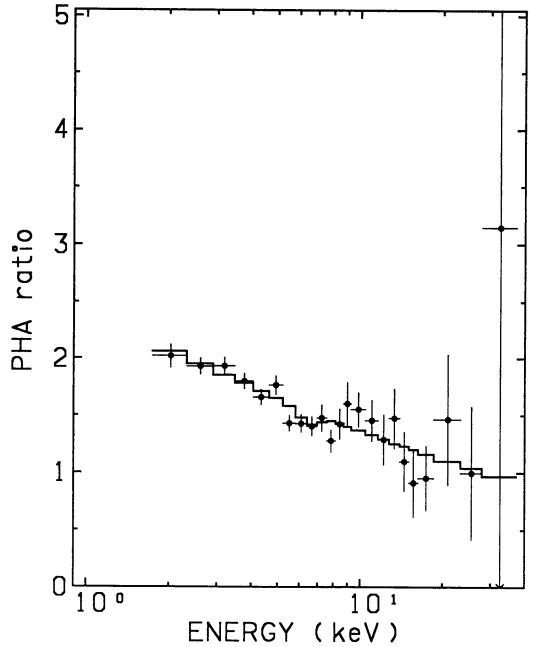

FIG. 4.—Pulse height ratio of the high-intensity and low-intensity spectra of MCG −6-30-15. The reduced chi-square for a constant is $\chi^2_\nu = 5.5$ with $\nu = 22$. The continuous line ($\chi^2_\nu = 0.9$) is the expected ratio obtained by fitting the spectra with C and α as free parameter and $N_{\rm H}$, $N_{\rm HFe}$, and $I_{\rm Fe}$ fixed to their mean values.

In all the models presented in Table 2, the spectral index of the (primary) power law is the only parameter which shows a significant correlation with the intensity level. We investigated in more detail this behavior, analyzing the spectra of the 17 single orbits separately. Our aim was to confirm that the observed spectral variations were really produced by changes of the spectral index and not by variations of low-energy absorption. Each spectrum was fitted in the 2–20 keV range by a power law, with C, α, and $N_{\rm H}$ as free parameters, whereas the iron absorption edge and emission line were fixed to the mean values given in Table 2A. This model provides a good fit to the spectra of single orbits, that have a lower statistics than summed spectra. Then we performed a correlation test on the α versus count rate and $N_{\rm H}$ versus count rate distributions. Only the spectral index shows a significant correlation with the count rate, with the correlation coefficient, $r = 0.64$, corresponding to a probability of a random fluctuation from uncorrelated variables $P(|r| > 0.64) = 5.6 \times 10^{-3}$. No correlation between $N_{\rm H}$ and the count rate is present ($r = -0.10$, $P(|r| > 0.10) = 0.70$).

As a final check we performed two sets of fit on the spectra of single orbits, the first one with α (and C) as free parameters and $N_{\rm H}$ fixed to the mean value of Table 2A, and the second one with $N_{\rm H}$ (and C) as free parameters and α fixed to the mean value of 1.66. In both cases we again fixed the iron absorption edge and emission line to their mean values. Then, for each orbit, we compared the resulting χ^2, assuming a minimum significant difference of $\Delta\chi^2 = 1$. We found that fits with α as free parameter were preferred in 12 cases, those with $N_{\rm H}$ as free parameter in one case, and there was no significant difference ($\Delta\chi^2 < 1$) in four cases.

We conclude that the spectral variations observed in MCG −6-30-15 are well described by spectral index changes. This is clear in Figure 4, where, along with the observed pulse height ratio between the high-intensity and low-intensity spectra, we plot the expected ratio obtained by fitting these spectra with the previous model with only normalization and spectral index as free parameters. The agreement is good ($\chi^2_\nu = 0.9$).

In Figure 5 we show the α versus unabsorbed 2–10 keV flux (F_c in 10^{-11} ergs cm^{-2} s^{-1} units) contained from the fits with $N_{\rm H}$ fixed. The correlation coefficient $r = 0.74$ corresponds to a probability $P(|r| > 0.74) = 7 \times 10^{-4}$ of being a random fluctuation. Moreover the reduced χ^2 for a constant is $\chi^2_\nu = 2.9$ with $\nu = 16$, whereas the best-fit linear relationship:

$$\alpha = 1.23(\pm 0.09) + 0.081(\pm 0.016)F_c \qquad (3)$$

(in parenthesis 1 σ errors) gives $\chi^2_\nu = 1.4$ with $\nu = 15$. The F test shows that this improvement is significant at a 99.9% confidence level.

Similar results have been obtained by using the partial covering model with $f_{\rm cov}$ and $N_{\rm Hcov}$ fixed to the mean values of Table 2D. In this case the spectral indexes were slightly steeper ($\Delta\alpha \approx 0.07$), as it is evident by comparing the values of spectral indexes in Table 2B with those in Table 2A.

So far we have shown that the spectral variability observed in MCG −6-30-15 is well described by spectral index variations correlated with the intensity and not by variations in the low-energy absorption. Now we investigate whether the presence of the high-energy flatter component could reproduce the observed spectral variability. According to the light curves pre-

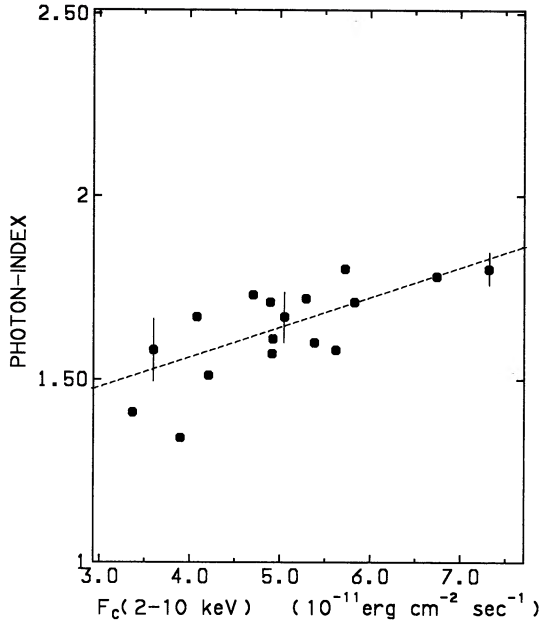

FIG. 5.—The correlation diagram of the spectral index and the unabsorbed 2–10 keV flux in MCG −6-30-15, obtained from spectra of 17 orbits. Typical errors of spectral index are indicated. The correlation coefficient $r = 0.74$ corresponds to a probability $P(|r| > 0.74) = 7 \times 10^{-4}$ of being a random fluctuation. The dashed line is the best-fit linear relationship.

sented in the next section, this component might be variable on longer time scales than the direct emission or even be constant. Its relative contribution will be therefore larger when the intensity of the source below 10 keV is lower, producing a flattening in the overall spectrum. In this hypothesis the spectral variability would be produced only by a change in the relative normalization of the hard and direct component. Could this effect reproduce also quantitatively the observed spectral variability? To test this hypothesis we fitted the low- and mid-level spectra with the reflection model (which is the most favorable, since its contribution at lower energies is greater than the partial covering model), keeping the spectral index fixed to the value observed for the high-level spectrum (Table 2D, third line), when the relative contribution of the hard component is the smallest by assumption. The column density was fixed to the average value of Table 2D. The other parameters, C, r, I_{Fe}, were free. The reduced χ^2 obtained for the low- and mid-level spectra were $\chi^2_\nu = 2.3$ and 1.5, respectively, definitely worse than those obtained with the spectral index as a free parameter. In fact, the covered and reflected component have a small effect on the flux below 10 keV, where instead larger spectral variations are observed, as shown in Figure 4.

In order to find other explanations for the spectral variability than that provided by spectral index changes we should resort to new spectral components, whose presence is, however, not required by the spectral data presented in § III*b*. An interesting possibility is suggested by the existence of a soft X-ray excess, detected in MCG −6-30-15 by the LE telescope (0.05–2 keV) aboard *EXOSAT* (Pounds, Turner, and Warwick 1986). Spectral variability could be produced by a change in the relative contribution of this steep component and the flatter power law. When the intensity is higher, the contribution of the soft component would increase, thus steepening the overall spectral shape. We tested this hypothesis by using a thermal bremsstrahlung, representing the soft excess, on the top of the harder emission produced by the power law and reflected component. The spectral index was fixed to the value obtained in the lower-level spectrum, when the contribution of the soft excess should be the smallest, as implied by the proposed explanation. The column density was fixed to the average value and the reflected/direct fraction to $r = 2.2$ (different values of r do not influence the results on spectral variability below 10 keV, as previously stressed). The other parameters, C, the normalization and temperature of the soft component, I_{Fe}, were free. The fits on the mid- and high-level spectra give χ^2_ν values as good as those obtained for the Compton reflection model with α free (not surprisingly since we have added an additional component). At 1 keV the flux of the thermal bremsstrahlung is ~50% (high-level spectrum) and 20% (mid-level spectrum) of the power-law emission. However, the temperature ($kT = 6.1 \pm 2.1$, 7.6 ± 3.6 keV, for the high- and mid-level spectra, respectively) are too high to be consistent with those observed in soft X-ray excesses ($kT \approx 0.1$ keV, see Piro *et al.* 1988 for a review). We will further discuss this results in § V*c*.

d) Temporal Behavior and Spectral Variability

In Figures 6*a*–6*c* we present the light curves of data used for spectral analysis integrated on one orbit (~10–20 min.) in the 1.7–4.6 keV, 4.6–10.5 keV, and 10.5–27.9 keV bands. The two bands below 10 keV can provide further information about the observed spectral variability. The light curves appear strongly correlated, as confirmed by a cross correlation analysis performed on the data with a minimum uninterrupted coverage of 1000 s and shown in Figure 7. Furthermore, no significant lag greater than a time bin (64 s) is present within 500 s. Lags greater than 500 s could not be detected because of the poor statistics and the temporal structure of data series (§ III*a*). Even though the shape of the light curves is the same, the amplitude of variations in the higher energy range is lower, as expected from the observed spectral variability (Fig. 4). All these results suggest that the spectral variability is produced by a single spectral component.

In Figure 6*c* we show the light curve in the 10.5–27.9 keV range. In this band the contribution of the covered or reflected component, and that of the direct power law are of the same order. As discussed in § V*a*, the light curve of the covered or reflected component should be a delayed and smoothed version of the light curve of the direct emission, with a lag determined by the size of the thick matter regions. Unfortunately, the statistical quality of data does not allow any significant conclusion. In the same figure we present the light curve expected in the extreme cases. In the first (*solid curve*) the two component are fully correlated (lag = 0). In the second case (*dashed curve*) the reflected or absorbed component is constant, that is the case when the size of the region is much larger than the observing time (lag > 2 days), thus smearing out all variations on shorter time scales. Both expected light curves are in agreement with data.

IV. NGC 4051

a) Light Curve

The X-ray flux of NGC 4051 was a factor of ~3 lower than that of MCG −6-30-15 but the temporal behavior was similar. In Figure 8, top panel, we show the light curve, corresponding to a total live time of ~40,000 s and with a time bin of 128 s. Large and erratic variations, up to a factor of 5, on all the time scales are evident. A similar behavior was observed by

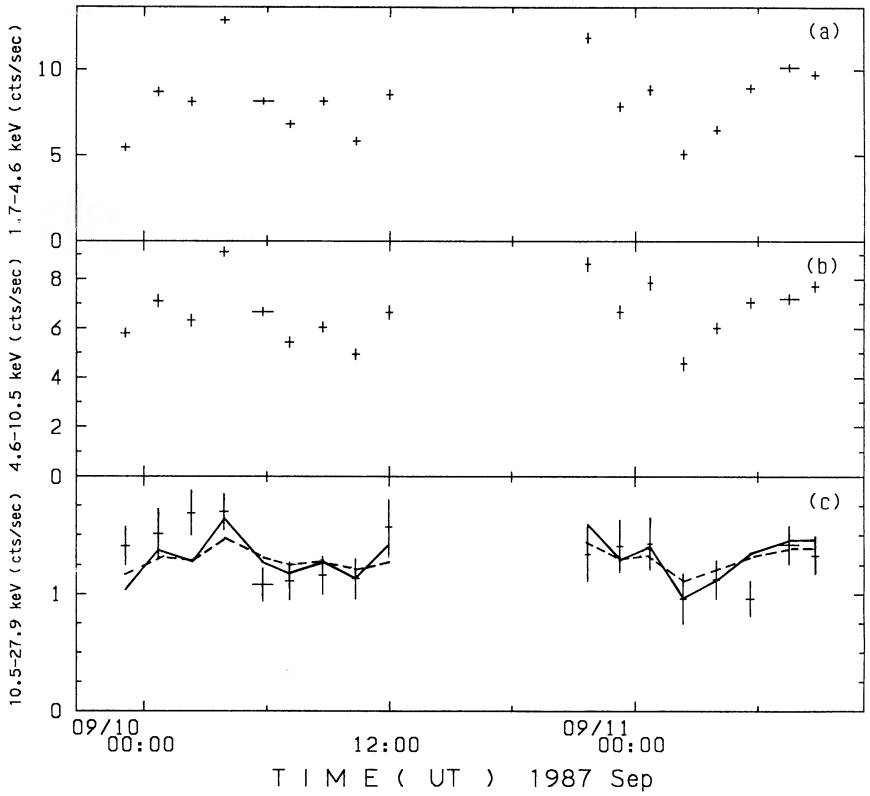

FIG. 6.—(*a*) Light curve of MCG −6-30-15 in the 1.7–4.6 keV energy range integrated on one orbit. (*b*) Same as (*a*) but in the 4.6–10.5 keV energy range. (*c*) Same as (*a*) but in the 10.5–27.9 keV energy range. The *solid* and *dashed curves* represent the light curves expected when the direct and reflected component are fully correlated (*solid curve*, lag = 0) and when the reflected component is constant (*dashed curve*, lag > 2 days).

EXOSAT (Lawrence *et al.* 1985) but, as for MCG −6-30-15, we were able to detect shorter time scales, as shown in Figure 8, bottom panel, where variations of 50%, on a time scale of few minutes, are present.

Likewise MCG −6-30-15, a power spectral density was obtained by summing independent power spectra of short data segment from 15 orbits (Fig. 9). Source power extends up to $\sim 5 \times 10^{-3}$ Hz, where the noise becomes dominant.

b) X-ray Spectrum

Spectra from 31 orbits were available for spectral analysis. Spectral variability, similar to that observed in MCG −6-30-15, is present also in this object, but the dynamics of amplitude variations is greater. Following a procedure similar to that used for MCG −6-30-15, we divided the spectra in four intensity levels (low, middle-low, middle-high, high). The corresponding count rate, integration time, and incident flux are listed in Table 3. This table also gives background exposure times and a mean background count rate.

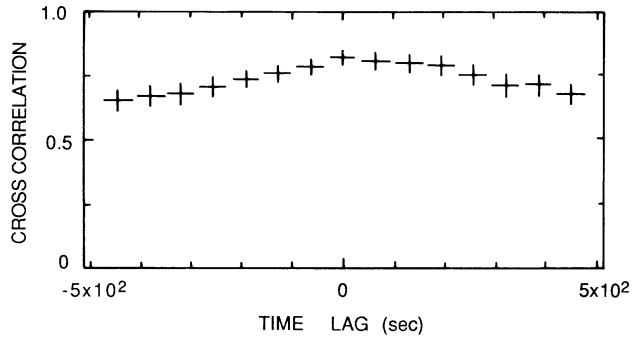

FIG. 7.—Cross correlation between the 4.6–10.5 keV and 1.7–4.6 keV time series of MCG −6-30-15 with a continuous observational period over 1000 s and a time bin of 64 s. Larger lags are not plotted because of the nature of *GINGA* timing data (see text).

Spectral fitting was performed in the energy range 2–37 keV and best-fit parameters and χ^2_ν obtained with different trial models are presented in Table 4. The best-fit simple power law to the middle-low intensity spectrum, that has the highest integration time, is shown in Figure 10*a*. Inspection of residuals shows some evidence of an iron line and iron edge, but the significance is not so strong as for MCG −6-30-15, that was 3 times brighter. Addition of a narrow line at 6.4 keV and iron edge at 7.1 keV yields to an improvement in χ^2_ν for the middle-low and middle-high intensity spectra. The results, listed in Table 4A, can be compared with those obtained in MCG −6-30-15 using the same model. They are similar in the presence of a high iron column density, $N_{\rm HFe} = (4 \pm 2) \times 10^{22}$ cm^{-2}, with no equivalent absorption at low energies ($N_{\rm H} < 0.3 \times 10^{22}$ cm^{-2}). This result would indicate that the physical and geometrical condition of the absorbing matter in NGC 4051 is similar to that in MCG −6-30-15. Hence we applied a partial covering model with solar abundance (eq. [1]) and the results, shown in Figure 6*b* for the middle-low intensity spectrum and listed in Table 4B for all the spectra, can be compared with those obtained for MCG −6-30-15 in Table 3B. The main difference is in the column density of the covered component, $N_{\rm Hcov} = (14^{+4}_{-2}) \times 10^{22}$ cm^{-2}, lower than that observed in MCG −6-30-15. However, we cannot exclude an additional, more heavily absorbed component because NGC 4051 was a factor of ~ 3 fainter than MCG −6-30-15 and data above 10

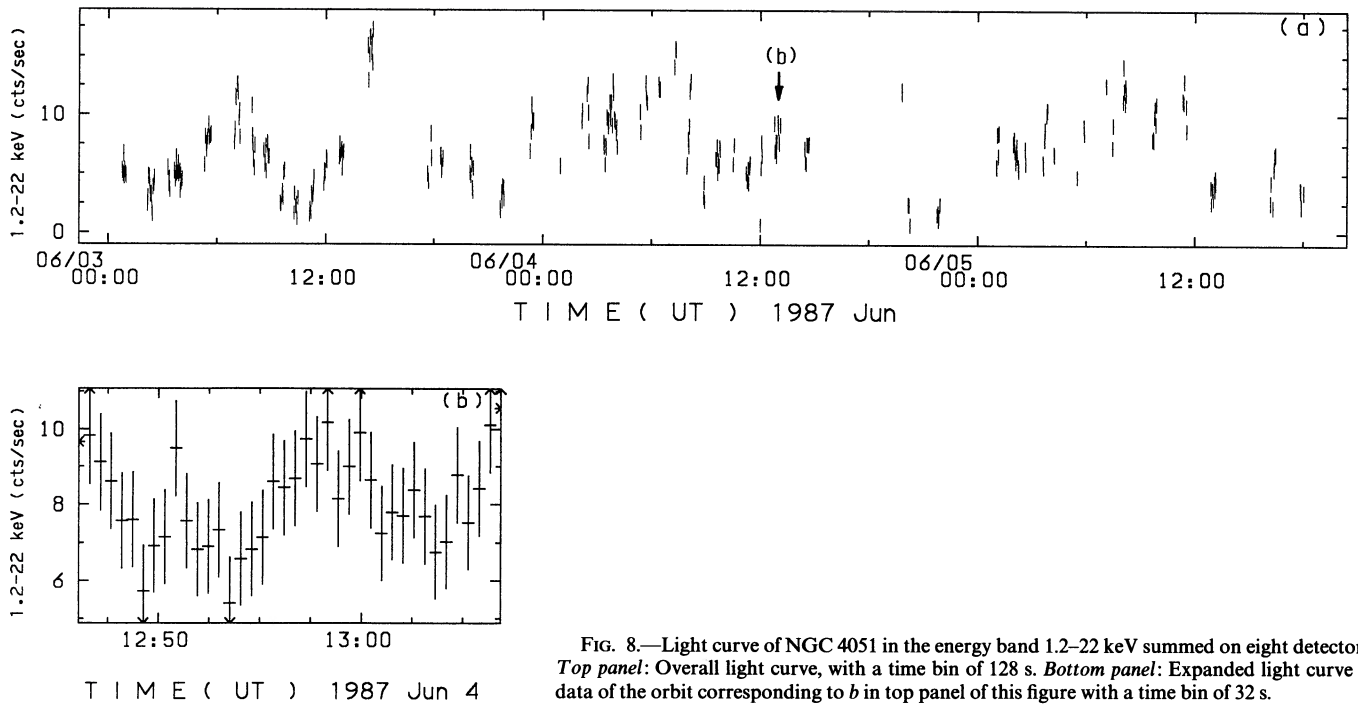

FIG. 8.—Light curve of NGC 4051 in the energy band 1.2–22 keV summed on eight detectors. *Top panel*: Overall light curve, with a time bin of 128 s. *Bottom panel*: Expanded light curve of data of the orbit corresponding to *b* in top panel of this figure with a time bin of 32 s.

keV, where a heavily absorbed component might show up, have a poorer statistics.

A fit with the Compton reflection model (2), presented in Table 4C, leads to the same conclusion. The normalization of the reflected component, mainly constrained by data above 8 keV, is consistent with zero, but also with a level similar to that of MCG −6-30-15.

Two-component models are not conclusive too. In the fit with a two–power-law model, the spectral indexes of the two components are practically the same, thus reducing to a simple power law. The thermal bremsstrahlung–power-law model (Table 4D) does not give any improvement in χ^2 compared to the simple power law.

We conclude that the signal-to-noise ratio of the spectra of NGC 4051 is too low to constrain the values of parameters of complex models.

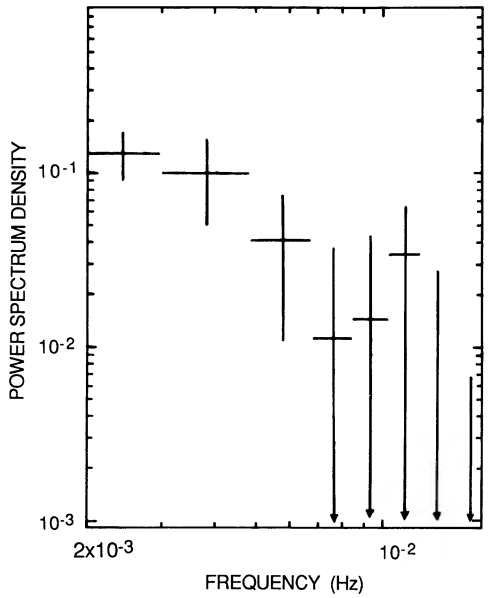

FIG. 9.—Power spectrum of NGC 4051 in the same energy range as Fig. 8. Poissonian noise power is subtracted in this figure.

c) *Spectral Variability*

Spectral variability, like that observed in MCG −60-30-15, is also present in NGC 4051. In Figure 11 the pulse height ratio between the high and middle-low intensity spectra is shown. The ratio is not consistent with a constant ($\chi^2_\nu = 3.7$) and indicates that the spectrum becomes steeper when the intensity is higher.

To analyze in more detail this behavior, we fitted the 31 spectra of single orbits with a simple power law in the 2–20 keV range, with C, α, and N_H as free parameters. This model provides a satisfactory fit to the spectra of single orbits. We found a significant correlation between the spectral index and the count rate ($r = 0.55$, $P(|r| > 0.55) = 4 \times 10^{-3}$), whereas no correlation between N_H and count rate is present [$r = -0.13$, $P(|r| > 0.13) = 0.5$], the absorption column density being consistent with the mean value $N_H = (0.60 \pm 0.25) \times 10^{22}$ cm^{-2}.

We verified this behavior with a different method. We performed two sets of fit on the spectra of single orbits, the first one with α (and C) as free parameters and N_H fixed to the mean value of 6×10^{21} cm^{-2}, and the second one with N_H (and C) as free parameters and α fixed to the mean value of 1.83. Then, for each orbit, we compared the resulting χ^2, assuming a minimum significant difference of $\Delta\chi^2 = 1$. We found that the fits with α as free parameters were preferred in 11 cases, those with N_H as free parameter in four cases and there was no significant difference ($\Delta\chi^2 < 1$) in 16 cases. We conclude that the spectral variations observed in this object are well described by changes in the spectral index of a simple power law. This is also shown in Figure 11, where, along with the observed pulse height ratio between the high-intensity and middle-low intensity spectra,

TABLE 3

COUNT RATE, EFFECTIVE EXPOSURE TIME AND INCIDENT FLUX OF THE SPECTRA OF NGC 4051 SUMMED IN FOUR INTENSITY LEVELS

	SOURCE				
	Count Rate[a] (counts s^{-1})		Exposure Time[b]		BACKGROUND[d] EXPOSURE TIME
LEVEL	Range	Mean	(s)	F(2–10 keV)[c]	(s)
Low	3.0–5.0	3.8	7035	0.9	7593
Mid-Low	5.0–7.5	6.2	10932	1.5	10634
Mid-High	7.5–10	8.8	7482	1.9	6527
High	10–15	11.9	4719	2.7	6241

[a] Count rate in the 2–20 keV range summed on eight detectors.
[b] The exposure time is not corrected for the collimator efficiency, corresponding to ~92%.
[c] The incident flux (10^{-11} ergs cm^{-2} s^{-1}) is independent from the model within 5%.
[d] Background level is similar for the four spectra and corresponds to ~44 counts s^{-1} for eight detectors.

we plot the expected ratio obtained by fitting these spectra with a simple power law with normalization and spectral index as free parameters and column density fixed to the mean value. The agreement is good ($\chi^2_\nu = 1.0$).

In Figure 12 we show the α versus unabsorbed 2–10 keV flux (F_c in 10^{-11} ergs cm^{-2} s^{-1} units) plot obtained from the fits with N_H fixed to the mean value. The correlation coefficient $r = 0.62$ corresponds to a probability of a chance occurrence $P(|r| > 0.62) = 2 \times 10^{-4}$. Moreover, the reduced chi square for a constant is $\chi^2_\nu = 2.2$ with $\nu = 30$, whereas the best-fit linear relationship,

$$\alpha = 1.35(\pm 0.10) + 0.21(\pm 0.04) \times F_c \,, \quad (4)$$

(in parenthesis 1 σ errors) gives $\chi^2_\nu = 1.4$ with $\nu = 29$. The F test (e.g., Bevington 1969) shows that this improvement is significant at more than 99.9% confidence level.

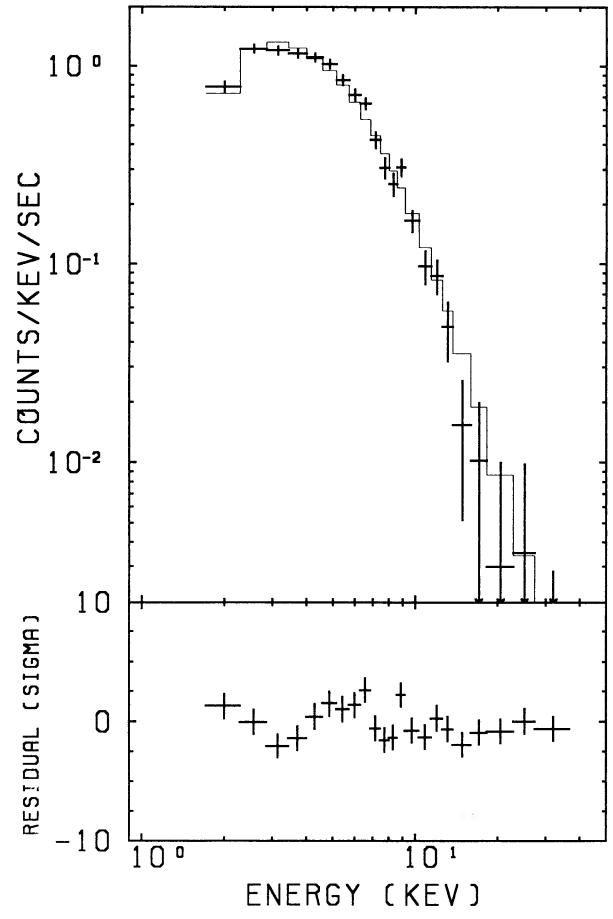

FIG. 10a

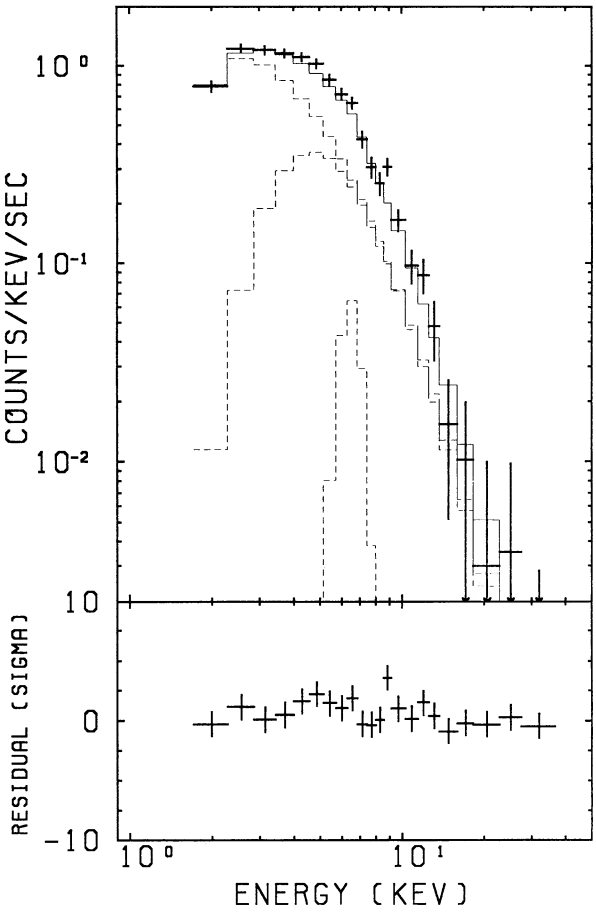

FIG. 10b

FIG. 10.—(*a*) Fit of a power law with uniform cold absorber to the mid-low intensity level spectrum of NGC 4051 ($\chi^2_\nu = 2.0$ with $\nu = 19$). (*b*) Same as in Fig. 6*a* but with a fit of partial covering model with solar abundances and narrow iron line.

TABLE 4

SPECTRAL FITS TO THE SPECTRA OF NGC 4051

A. POWER LAW WITHOUT AND WITH IRON FEATURES

Level	C^a	α^b	$N_H{}^c$	$N_{HFe}{}^d$	$I_{Fe}{}^e$	χ^2_ν
			Without ($\nu = 19$) Iron Features			
Low	2.5 ± 1.2	1.67 ± 0.27	$2.2^{+1.8}_{-1.5}$	...	...	1.2
Mid-Low	4.1 ± 0.8	1.73 ± 0.11	$1.0^{+0.4}_{-0.5}$	...	...	1.6
Mid-High	5.4 ± 1.1	1.79 ± 0.10	$0.2^{+0.5}_{-0.2}$	...	...	1.1
High	10.5 ± 1.7	1.96 ± 0.09	$0.5^{+0.4}_{-0.3}$	...	...	1.2
Mean	...	1.83 ± 0.06	0.60 ± 0.25	...	...	...
			With ($\nu = 17$) Iron Features			
Low	2.2 ± 1.0	1.62 ± 0.24	$0.0^{+2.0}_{-0.0}$	16^{+12}_{-16}	0.27 ± 0.35	1.1
Mid-Low	4.0 ± 0.7	1.74 ± 0.11	$0.0^{+1.0}_{-0.0}$	7^{+4}_{-3}	0.40 ± 0.25	1.3
Mid-High	5.7 ± 1.1	1.82 ± 0.12	$0.0^{+0.3}_{-0.0}$	2^{+3}_{-2}	0.45 ± 0.27	0.9
High	10.4 ± 1.6	1.96 ± 0.09	$0.0^{+0.5}_{-0.0}$	4^{+4}_{-3}	0.10 ± 0.35	1.2
Mean	...	1.84 ± 0.06	$0.0^{+0.3}_{-0.0}$	4 ± 2	0.34 ± 0.14	...

B. POWER LAW WITH PARTIAL COVERING AND SOLAR ABUNDANCES ($\nu = 16$)

Level	$C^{a,f}$	α^b	$N_H{}^c$	$N_{Hcov}{}^c$	$I_{Fe}{}^{e,f}$	f_{cov}	χ^2_ν
Low	2.5 ± 1.5	2.38 ± 0.45	$0.0^{+0.3}_{-0.0}$	16^{+5}_{-3}	0.10 ± 0.42	0.78 ± 0.10	0.8
Mid-Low	4.8 ± 1.3	2.21 ± 0.28	$0.3^{+0.7}_{-0.3}$	13^{+12}_{-7}	0.25 ± 0.27	0.54 ± 0.20	0.9
Mid-High	5.7 ± 1.4	1.91 ± 0.26	$0.1^{+0.3}_{-0.1}$	8^{+22}_{-4}	0.42 ± 0.30	0.23 ± 0.26	0.9
High	11.5 ± 2.0	2.25 ± 0.22	$0.2^{+0.3}_{-0.2}$	10^{+9}_{-5}	0.00 ± 0.37	0.43 ± 0.19	1.0
Mean	...	2.16 ± 0.14	$0.1^{+0.2}_{-0.1}$	14^{+4}_{-2}	0.23 ± 0.16	0.64 ± 0.08	...

C. REFLECTION MODEL ($\nu = 17$)

Level	$C^{a,f}$	α^b	$N_H{}^c$	r^g	$I_{Fe}{}^{e,f}$	χ^2_ν
Low	2.5 ± 1.4	1.71 ± 0.29	2.0 ± 1.0	$0.1^{+4.2}_{-0.1}$	0.31 ± 0.31	1.2
Mid-Low	4.3 ± 1.6	1.78 ± 0.14	$0.9^{+0.6}_{-0.4}$	$0.0^{+4.0}_{-0.0}$	0.45 ± 0.25	1.3
Mid-High	6.0 ± 2.0	1.87 ± 0.15	$0.3^{+0.7}_{-0.2}$	$0.3^{+3.7}_{-0.3}$	0.47 ± 0.34	0.9
High	11.5 ± 2.8	2.03 ± 0.12	$0.6^{+0.8}_{-0.4}$	$0.4^{+4.3}_{-0.4}$	0.37 ± 0.15	1.2
Mean	...	1.90 ± 0.08	$0.7^{+0.4}_{-0.2}$	$0.2^{+2.0}_{-0.2}$	0.39 ± 0.11	...

D. THERMAL BREMSSTRAHLUNG POWER LAW ($\nu = 16$)

Level	$C_1{}^a$	κT^h	$N_H{}^c$	$C_2{}^a$	$\alpha_2{}^b$	$I_{Fe}{}^e$	χ^2_ν
Low	1.8 ± 1.0	17.0 ± 5.0	$1.6^{+2.0}_{-1.0}$	0.17 ± 0.10	$1.2^{+1.8}_{-1.2}$	0.27 ± 0.35	1.3
Mid-Low	3.2 ± 1.0	$18.3^{+7.0}_{-9.5}$	$0.5^{+0.4}_{-0.3}$	$0.0^{+0.14}_{-0.0}$	$0.9^{+2.1}_{-1.3}$	0.50 ± 0.22	1.2
Mid-High	2.9 ± 2.9	$6.3^{+15}_{-6.0}$	$0.1^{+0.8}_{-0.1}$	1.7 ± 1.0	$1.4^{+0.6}_{-1.5}$	0.45 ± 0.35	1.0
High	8.0 ± 1.6	$8.2^{+5.0}_{-3.0}$	$0.2^{+0.5}_{-0.1}$	$0.0^{+0.1}_{-0.0}$	$0.0^{+2.0}_{-1.0}$	0.25 ± 0.35	1.0
Mean	...	$12.0^{+3.1}_{-2.3}$	$0.3^{+0.4}_{-0.1}$	...	$0.5^{+0.7}_{-0.2}$	0.40 ± 0.15	...

NOTES.—Range of fit 2–37 keV. Errors are 90% confidence level for one interesting parameter.

[a] Normalization in 10^{-3} photons cm^{-2} s^{-1} keV^{-1} at 1 keV.

[b] Photon index.

[c] Column density in 10^{22} cm^{-2}.

[d] $N_{HFe} = N_{Fe} \times 10^{4.48}$ in 10^{22} cm^{-2}. The iron cross section includes both the K and L shell absorption.

[e] Line intensity in 10^{-4} photons cm^{-2} s^{-1}.

[f] Normalization of the uncovered or direct component.

[g] Normalization of the reflected component relative to the direct component (eq. [2]).

[h] Temperature in keV.

We investigated other explanations for the spectral variability. As with MCG −6-30-15, we fitted the low-intensity spectra with the reflection model with the spectral index fixed to the value observed in the high-intensity level ($\alpha = 2.03$). Again the values of χ^2_ν ($\chi^2_\nu = 1.6$, 2.0 for the low- and mid-low intensity spectra) rule out this possibility.

A varying contribution of a thermal bremsstrahlung component on the top of a flat power law ($\alpha = 1.67$) provides instead a satisfactory result in terms of the quality of the fits. At 1 keV the flux of the thermal bremsstrahlung component is about the same of the power-law emission in the high-intensity level. However, the temperature of 3.5 ± 1.4 keV is too high to identify this component with a soft X-ray excess.

Finally we note that, unlike MCG −6-30-15, the absorbed component in the partial covering model might have a fairly large effect below 10 keV (Fig. 10*b*). Spectral variability could be produced by a variation of the covering fraction or, more generally, by changes in the physical or geometrical structure of the absorbing matter, correlated with the luminosity. In fact, whereas in power-law fits there is a definite evidence for a

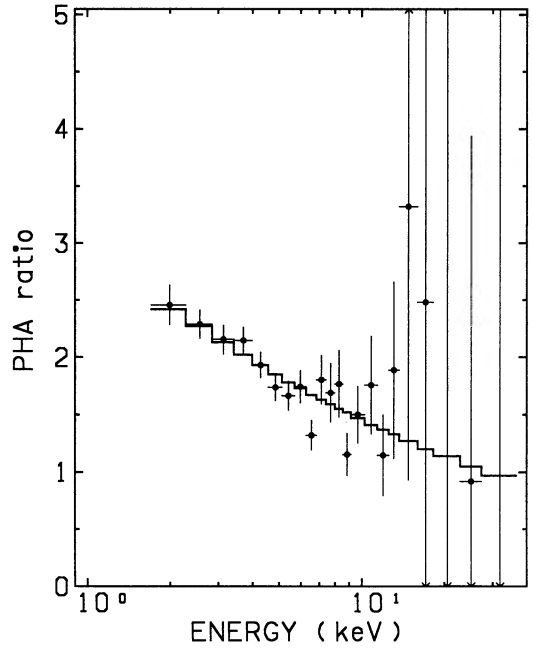

FIG. 11.—Pulse height ratio of the high-intensity and middle-low intensity spectra of NGC 4051. The reduced chi square for a constant is $\chi^2_\nu = 3.7$ with $\nu = 21$. The dashed line ($\chi^2_\nu = 1.0$) is the expected ratio obtained by fitting the spectra with C and α as free parameter and N_H fixed to the mean value.

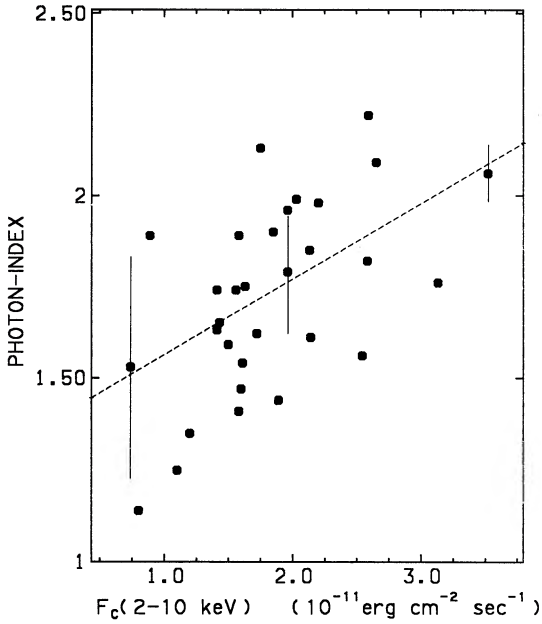

FIG. 12.—The correlation diagram of the spectral index and the unabsorbed 2–10 keV flux in NGC 4051, obtained from spectra of 31 orbits. Typical error bars for the spectral index are indicated. The correlation coefficient $r = 0.62$ corresponds to a probability $P(|r| > 0.62) = 2 \times 10^{-4}$ of being a random fluctuation. The dotted line is the best-fit linear relationship.

correlation between the spectral index and intensity, no correlation between α or any other relevant parameter and intensity is evident using a partial covering model (Table 4B). This is not surprising, given the low statistics and the number of free parameters used in this model. More definite conclusions could be derived in future observations with a greater sensitivity or with the source in a higher level.

d) Temporal Behavior and Spectral Variability

In Figure 13 we present the light curves in the 1.7–4.6 keV and 4.6–10.5 keV energy bands. Each point corresponds to the average value of data for each orbit. The signal to noise ratio is too small to provide an useful light curve above 10 keV. The light curves do not show any appreciable difference, but the amplitude of variations, like MCG −6-30-15, is lower in the higher energy range. A cross correlation analysis with a smaller time bin (64 s) on data selected as described in § IV*a* does not show any significant lag greater than one time bin (Fig. 14). A correlation of the light curves of two energy bands is similar to that obtained for MCG −6-30-15 (Fig. 7).

V. DISCUSSION AND CONCLUSIONS

a) Temporal Behavior

EXOSAT observations of MCG −6-30-15 (Pounds and Turner 1986; Pounds, Turner, and Warwick 1986) and NGC 4051 (Lawrence *et al.* 1985, 1987) showed light curves charac-

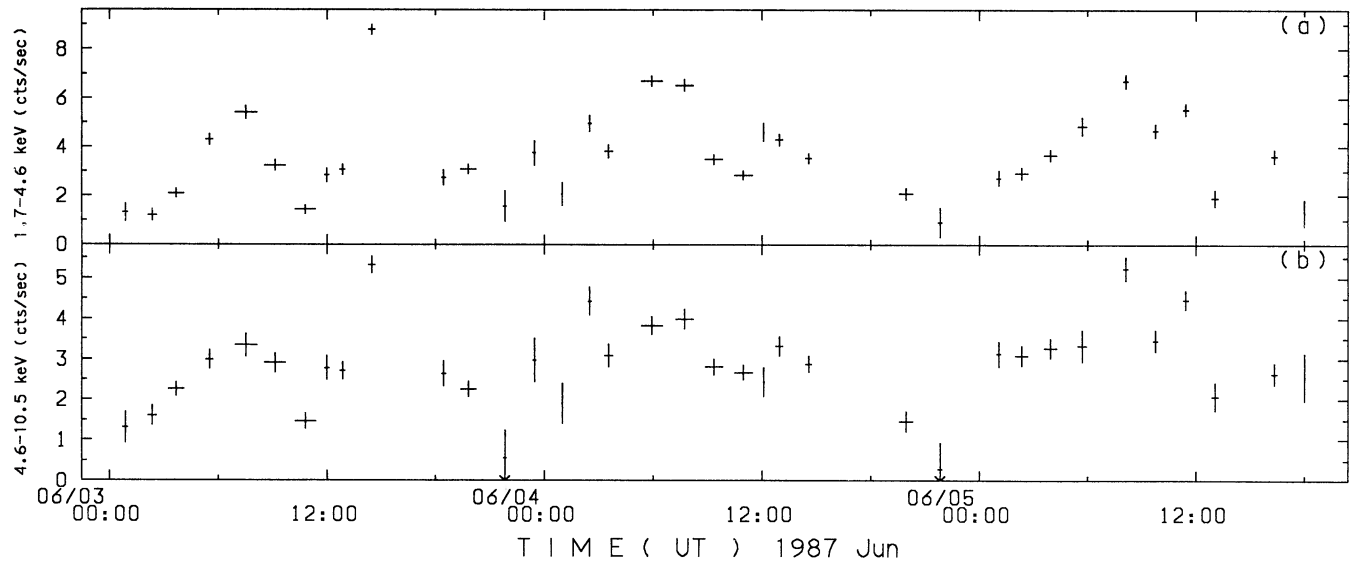

FIG. 13.—(*a*) Light curve of NGC 4051 in the 1.7–4.6 keV energy range integrated on one orbit. (*b*) Same as (*a*) but in the 4.6–10.5 keV energy range.

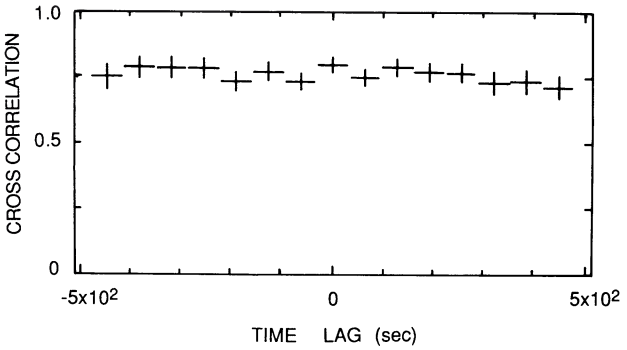

FIG. 14.—Cross correlation between the 4.6–10.5 keV and 1.7–4.6 keV time series of NGC 4051 with a continuous observational period over 1000 s and a time bin of 64 s. The light curves are well correlated, with no significant lag between 64 s and 500 s. Larger lags are not plotted due to the nature of *GINGA* timing data (see text).

terized by variations of similar amplitude on all time scales down to 1000 s, where the Poissonian noise becomes dominant. The corresponding power spectra follow a frequency^{-1} distribution.

The light curves obtained by *GINGA* are qualitatively similar to those observed by *EXOSAT*, in the presence of large and erratic variations, but the structure of *GINGA* time series does not allow a more direct comparison based on a power spectral analysis. On the other hand, the larger area and lower background of the LAC provided evidence of large intensity variations ($>50\%$) on time scales as short as 200 s. Below this limit the Poissonian noise becomes dominant. We conclude that a "shortest" time scale of variability, that could be associated with, for example, light travel time across the emitting region or dynamical time scale around a black hole, remains still undetected. Neverthess, the upper limit of 200 s can be used to constrain the black hole mass of the two objects. In the assumption that short time-scale variations are produced in the innermost stable orbit of a Schwarzschild black hole, the light crossing time argument indicates masses less than 4×10^6 solar masses.

b) The X-ray-Absorbing Matter in MCG −6-30-15 and NGC 4051

The iron abundance in MCG −6-30-15 as obtained by a simple power-law model with uniform absorber, would be at least 10–20 times greater than the solar value. A similar evidence, but with a lower statistical significance compared to the *GINGA* data, has been found in a long *EXOSAT* observation of MCG −6-30-15 by Nandra *et al.* (1989). Such a strong iron overabundance seems unlikely. There are two other AGNs that show an iron edge in their X-ray spectra, namely, Centaurus A and NGC 4151. In Centaurus A (Wang *et al.* 1986) the iron abundance is consistent with the solar value, whereas in NGC 4151 measurements from different satellites give values 2–3 times greater than the solar one (e.g., Holt *et al.* 1980; Perola *et al.* 1986; Matsuoka *et al.* 1986; Warwick *et al.* 1989*b*).

An alternative and more attractive explanation for such an enhanced edge would obtain if the medium is highly ionized by the X-ray continuum. Our results imply that the ratio of opacities at low energies ($\sim$2–4 keV) and at the iron edge is at least a factor of ~ 10 lower than the corresponding ratio in the cold case. In presence of ionization the opacity to soft X-ray photons is reduced more than the opacity to hard photons, mainly because the lighter atoms, which dominate the photoelectric absorption at lower energies, are fully ionized. This model could therefore provide the required reduction of opacity at low energies if there were the matter enough ionized. On the other hand, we can put an upper limit to the ionization state of matter from the observed energies of the iron edge and line. They correspond to an iron ionization state less than the XVIII, that implies $\xi < 100$ ergs cm s^{-1} and $T < 10^5$ K (Kallman and McCray 1982), where $\xi = L/(nr^2)$ (or $\Xi = L/(4\pi cnr^2kT)$) is the photoionization parameter, L is the luminosity of the ionizing continuum, and r, n, and T are the distance from the continuum source, density, and temperature of the gas, respectively. The opacity of a photoionized gas with solar abundances has been computed by Krolik and Kallman (1984) and is shown in Figure 4 of their paper for some photoionization parameters. Our upper limit corresponds to the curve at $\Xi = 13.3$, $T = 9.1 \times 10^4$ K ($\xi \simeq 100$ ergs cm s^{-1}) but in this case the reduction in opacity at low energies is only a factor of 2–3 compared to the cold case. We conclude that a model based on a simple power-law continuum absorbed by a photoionization medium with solar abundances cannot explain the X-ray spectrum of MCG −6-30-15, and that the deviations from a simple power law (Fig. 3*a*) observed above 7 keV are produced by a complex spectral shape.

Then we consider the most natural modification to the cold uniform absorber model, in which the absorbing medium does not fully cover the continuum region. Solar abundances were assumed. This medium is usually identified with the clouds of the broad-line region (BLR) (e.g., Mushotzky 1984*b*; Reichert, Mushotzky, and Holt 1986), known from optical observations (Kwan and Krolik 1981) to have column densities of the order of 10^{22}–10^{23} cm^{-2}, similar to those observed in X-ray spectra. This "leaky" absorber or partial covering model was introduced by Holt *et al.* (1980) to explain the soft excess above the uniform absorption model in the *Einstein*/SSS spectrum of NGC 4151 and applied more recently by Perola *et al.* (1986), Pounds *et al.* (1986), and Warwick *et al.* (1989) to *EXOSAT* and *GINGA* observations of this galaxy. A similar spectral behavior was observed in other AGNs by Reichert *et al.* (1985).

The results of the fit with a partial covering model to the spectrum of MCG −6-30-15 were rather unexpected and hardly fit the equation BLR = X-ray absorber. In fact, they indicate that a rather great fraction of the source (up to 60%) is covered by a very thick absorber, with a derived column density of $\sim 3 \times 10^{24}$ cm^{-2} (that effects of scattering increase to the observed value of 6×10^{24} cm^{-2}), one order of magnitude greater than that of the BLR clouds.

A medium with such (or greater) column density can produce effects on the spectrum even if it is not along our line of sight toward the central object, as required in the partial covering model. In fact matter in the environment of the central source can intercept and reprocess, through Compton scattering and absorption (and fluorescence) processes, a great fraction of the nuclear emission (Lightman and White 1988; Guilbert and Rees 1988). We found that a model composed by a direct and reflected (reprocessed) component provides an equally good fit to the spectrum of MCG −6-30-15.

Both the partial covering and reflection model indicate that the main deviations of the observed continuum from a simple power law are produced by a spectral flattening above 8–10 keV, where the covered or reflected component become comparable to the direct emission. We investigated whether this spectral shape might be produced by a complex continuum emission rather than by the effects of thick and inhomogeneous

matter. We used a power law–power law fit and thermal bremsstrahlung–power law fit to model the emission. Both fits required a very flat ($\alpha < 0$) hard power law, which dominates the spectrum above 10 keV. However, the hard component is too flat to be consistent with the spectral index of Seyfert galaxies above 30 keV (Rothschild *et al.* 1983) and the extrapolated flux would be much greater than that observed at this energies. Furthermore, these models give χ^2 values slightly worse than those obtained with the partial covering and reflection model. The spectral flattening observed by *GINGA* can be reconciled with the higher energy measurements only if the hard component recovers a steeper spectral index above 30–40 keV, as in the case of the partial covering and reflection models. These last models also provide a self-consistent explanation to the observed iron line, as discussed below. We conclude that the partial covering and reflection models give the most likely (given the best χ^2 values), and natural explanation to the spectrum of MCG −6-30-15. We will thus discuss in more detail the physical implications of the results obtained with these models.

Both models require the existence of a very thick medium, with $N_H \approx 10^{24}$ cm^{-2} for the partial covering model or greater for the reflection model. An additional uniform screen, covering the entire source with a column density of $\sim(6\text{–}8) \times 10^{21}$ cm^{-2}, is also required by our fits. This uniform absorber could be identified with the interstellar matter within the host galaxy, with a column density of $(4\text{–}10) \times 10^{21}$ cm^{-2}, as estimated by optical observation (Pounds, Turner, and Warwick 1986, and references therein).

The origin and location of the thick medium is more puzzling. Here we examine some possibilities about its origin. First we note that the ideal of very thick absorbers is not a new one. It was suggested (e.g., Lawrence and Elvis 1982) that Seyfert 2 galaxies have type 1 nuclei hidden by a thick screen. This suggestion was supported by optical and X-ray observations of NGC 1068 (Antonucci and Miller 1985; Koyama *et al.* 1989), the prototype of Seyfert 2 galaxies. In this object the line of sight to the active nucleus is completely obscured by a thick medium ($N_H > 10^{24}$–10^{25} cm^{-2}), probably a torus with the plane lying in our line of sight, and we see only a fraction of the central flux scattered by electrons in a cloud surrounding the nucleus. According to this interpretation, a thick torus should thus exist in some (possibly all) Seyfert 1 galaxies. Depending on the inclination of the torus, we would observe a Seyfert galaxy as type 1 (torus face on) or type 2 (torus edge on). In the framework of the partial covering model, MCG −60-30-15 might be a transition object between type 1 and 2 Seyfert galaxies, with only a fraction of the central source covered by this thick screen. A problem of this interpretation is the low probability of observing the central source partially covered. In fact, the absorbing screen has to cover the BLR and is therefore much larger than the central source. Hence, the central source would appear partially covered only within a very small solid angle, and MCG −6-30-15 should be a unique example of this situation. On the other hand, the existence of a heavily absorbed component, similar to that observed in MCG −6-30-15, has been detected in the *GINGA* spectrum of two other Seyfert galaxies, namely, NGC 7469 and IC 3229*a* (Piro, Yamauchi, and Matsuoka 1990; Piro, Matsuoka, and Yamauchi 1989), weakening this interpretation. Such a problem does not exist for the reflection model, because the reprocessing medium is not constrained to lie between us and the central source.

Another more attractive possibility is suggested by the existence of a soft X-ray nuclear excess in this object (Pounds, Turner, and Warwick 1986), widely recognized as the spectral signature of an accretion disk (e.g., Arnaud *et al.* 1985). The matter in an accretion disk can, in fact, be relatively cold ($T < 10^5$ K) and have column density of 10^{24}–10^{25} cm^{-2} within a wide range of radii (e.g., the standard disk model of Shakura and Sunyaev 1973). Such a disk might cover a rather great fraction of the central source that produces the X-ray continuum. For example, for a spherical source and a geometrically thin disk, the maximum covering fraction of 0.5 obtains when the disk is almost edge-on. On the contrary, a reflected component should be larger when the disk is face-on. The relatively large level of the covered and reflected component observed in MCG −60-30-15 is consistent with these extreme cases. Alternatively, accreting matter nearby the black hole could be in the form of lowly ionized clouds with column densities of the order of 10^{24}–10^{25} cm^{-2} (Guilbert and Rees 1988; Ferland and Rees 1988).

Information on the size of the thick matter region could be, in principle, extracted from the temporal behavior of the covered or reflected component. Photons reflected by matter at a distance d from the central source follow a longer path length than those emitted directly into our direction. We thus expect the light curve of the reflected component to be a delayed and smoothed version of the direct one, with a lag of the order of d/c. A similar effect is expected for the covered component. Even though the absorbing matter is located along our line of sight, scattering will increase the path length of photons by a factor of $\tau_T \Delta r = 2\Delta r$, where Δr is the thickness of the region. Unfortunately the statistics of light curves above 10 keV, where the contribution of the covered or reflected component is of the same order of the direct one, is poor and does not allow any definite conclusion.

In NGC 4051 a fit with a simple power-law model with a uniform cold absorber yields results similar to those obtained for MCG −6-30-15, with the presence of an iron line and some evidence for an iron edge, with no equivalent absorption at lower energies. These similarities would suggest the presence of a covered or reflected component by a very thick medium, as in the case of MCG −6-30-15. However, a fit with a partial covering model would indicate that the covered component is less absorbed than that of MCG −6-30-15, with a column density of $\sim 10^{23}$ cm^{-2}, consistent with the value of the BLR clouds. On the other hand, given the poorer signal, in particular at high energies, we cannot exclude the presence of an additional, more heavily absorbed component or a reflected component. Future observations, with the source in a higher level, should allow more definite conclusions.

The iron line emission can provide further informations on the matter surrounding the central source. First, it is important to understand whether the iron line emission is consistent with that expected from the partial covering and reflection model. If so, it is reasonable to assume that the medium producing the iron line is the same thick matter producing partial covering absorption or reflection, and use the iron line measurements to further constrain the physical condition and spatial distribution of this matter. In fact, other regions in the environment of the central "engine" could produce the iron line, such as the BLR (e.g., Perola *et al.* 1986).

In Table 5 we have summarized the relevant parameter of the iron line and continuum emission obtained in MCG −6-30-15. The statistics of spectra of NGC 4051 is too poor to

TABLE 5

IRON LINE AND CONTINUUM PARAMETERS IN MCG −6-30-15

LEVEL	I_{Fe}[a]	E.W.[b]	CONTINUUM FLUX (7.1–37 keV)[c] Direct	Reflected
Low	1.1 ± 0.4	280 ± 110	2.0	1.33
Mid	1.4 ± 0.4	290 ± 90	2.2	1.38
High	0.6 ± 0.5	100 ± 80	2.7	1.43

[a] Line intensity in 10^{-4} photons cm^{-2} s^{-1}.
[b] Equivalent width in eV.
[c] Flux of the direct and reflected component in 10^{-3} photons cm^{-2} s^{-1}. A typical uncertainty is ~50%.

produce significant results. We stress again that the line energy is just that expected from fluorescence emission from cold matter, as assumed in the partial covering and reflection models. The reflection model can also account for the observed level of the iron line. In particular, in a disk like geometry, an EW of 100–200 eV is expected (Basko 1978). For the partial covering model, a rough estimation obtains by using the results given in Leahy *et al.* (1989), referring to matter with very high column density in a spherical geometry. For $N_{Htrue} = 3 \times 10^{24}$ cm^{-2}, the EW relative to the covered component is ~10–20 keV. Since the direct component is 200 times greater than the covered one at 6.4 keV, the expected EW should be ~50–100 eV, slightly lower than observed.

A final point regards the correlation of the line intensity with the continuum level, which can provide an estimation of the size of the line emitting region (Perola *et al.* 1986). From Table 5 it appears that the intensity of the line does not correlate with the continuum level at 6.4 keV. In fact, the EW is not consistent with a constant. This result still holds when we consider the effect of spectral variability. In fact, the intensity of the line holds when we consider the effect of spectral variability. In fact, the intensity of the line should be compared with the photon flux above the iron K edge at 7.1 keV, which, as appears from Table 5 or Figure 4, is less variable than the continuum flux at lower energies. The intensity of the line would increase only by 30% from the low to the high state if it correlates with the continuum, which is still not consistent with the measurements. This result is not surprising, because we expect a lag between line intensity variations and continuum changes, determined by the size of the line emitting region. Since the continuum is varying on time scales as short as several minutes, we conclude that the size of the line emitting region should be greater than this value. We have also attempted to find a lag on time scales of hours, by using the single orbit spectra, but the corresponding errors on the line intensity are too large to give any significant result. In the framework of the reflection model we expect a direct correlation between the reflected component and the iron line, as they are produced by the same region through the reprocessing of primary radiation. Actually both the line intensity and the estimated flux of the reflected component (with a typical error of ~50%) listed in Table 5 are consistent with a constant.

A final comment regards the possibility that the thick matter is located nearby the central black hole, possibly in an accretion disk. In this case we would expect a Doppler broadening of the line due to the Keplerian motion of 10%–20% (corresponding to regions from ~10–50 Schwarzschild radii; see also Fabian *et al.* 1989), consistently with the possible detection of a broad line with a width of ~1 keV in MCG −6-30-15.

c) *Spectral Variability*

Another important result obtained from *GINGA* observations of MCG −6-30-15 and NGC 4051, is the detection of spectral variability in both objects. The spectral shape is a function of the luminosity, the spectrum being steeper when the source is higher. These variations are well reproduced by a change $\Delta\alpha \approx 0.3$–0.5, centered on $\alpha \approx 1.7$, when the luminosity increases by a factor of ~3–4.

There are other Seyfert galaxies showing spectral variability above 1 keV with the same correlation between spectral shape and luminosity. In these objects spectral variations are reproduced by changes in the spectral index as well. NGC 4051 itself, observed with *EXOSAT* by Lawrence *et al.* (1985), showed a positive correlation between the 2–6 keV flux and the softness ratio of CMA (0.05–2 keV) to ME (2–6 keV), that can be reproduced by a change of spectral index $\Delta\alpha \approx 0.3$ for a factor of 4 increase in the ME flux, consistently with our results. A positive correlation between spectral index and flux has also been observed in NGC 4151 (Perola *et al.* 1987) and NGC 5548 (Branduardi-Raymont 1986) by *EXOSAT* and in 3C 120 by *Einstein* (Halpern 1985). A similar, but less significant, correlation has been found in an *EXOSAT* observation of NGC 7314 by Turner (1987).

A much more enhanced spectral change ($\Delta\alpha > 2$) has been observed in the Seyfert 1 galaxy E1615+061, but its origin is probably due to an extremely variable soft X-ray excess superposed on the hard "canonical" component (Piro *et al.* 1988). In this object, the soft excess, at the highest level of intensity, extends and dominates the emission beyond 1 keV. We verified whether the spectral variations observed in MCG −6-30-15 and NGC 4051 might be produced by a variable soft X-ray excess, described by a thermal bremsstrahlung model, on the top of a hard spectrum of constant shape (§§ III*c* and IV*c*). The temperatures derived for the thermal component were $kT = 3.5$ keV and $kT = 6$–7 keV for NGC 4051 and MCG −6-30-15, respectively, much greater than those of soft X-ray excesses ($kT \approx 0.1$ keV; see Piro *et al.* 1988 for a review). This thermal component, if existing, cannot therefore be identified with a soft excess. Furthermore, it cannot explain the spectral shape observed in MCG −6-30-15, where the main deviations from a simple power law are produced by a high-energy bump. This spectral shape is, in fact, well fitted by a partial covering or reflection model, and no additional component is required from spectral fitting. Finally, if this component is of thermal origin, we would expect an iron line at 6.7 keV in the high state, when its contribution is of the same order of the hard power law. We conclude that there is no compelling evidence to include another new component in the spectra of these objects.

The presence of a hard component, possibly variable on longer time scales than the primary power law, again suggests an alternative to spectral index changes. For example, in the low state, the relative contribution of the covered or reflected component would be greater, thus producing a flatter overall spectrum. We have shown in § III*c* that this is not the case for MCG −6-30-15 at least, because the contribution of the covered or reflected component below 10 keV, where large spectral variations are observed, is too small.

Spectral variations similar to those observed in the present objects, might be produced by changes of opacity of a photoionization or "warm" absorber (Halpern 1984) in response to

variations of the ionizing flux. When the luminosity increases, the photoionization parameter increases and, correspondingly, the opacity to soft X-ray photons is reduced more than the opacity to hard X-ray photons, producing a steepening of the spectrum. This model has been proposed alternatively to spectral index changes, to explain the spectral variability in NGC 4151 (Yaqoob, Warwick, and Pounds 1988) and in the quasar MR 2251−178 (Pan, Stewart, and Pounds 1988) observed by *EXOSAT*. However, recent observations of NGC 4151 by *GINGA* (Yaqoob and Warwick 1989) have shown that spectral variations observed in this object cannot be reproduced by a warm absorber model, and that spectral index changes are necessary to fit the data. Furthermore, we have shown that a warm absorber model cannot explain the spectrum of MCG −6-30-15. This spectrum is well reproduced by a direct power-law continuum, partially covered or reflected by a cold and thick medium, that can also produce an iron line with energy and intensity in agreement with those observed. Thus, a warm absorber, whose presence is not required by the spectral fitting, should be introduced "ad hoc," in addition to the cold and thick medium, only to explain the spectral variability.

Regarding NGC 4051, we note that the spectral variability observed in this object is strikingly similar to that observed in MGC −6-30-15, suggesting the same physical origin.

All the observational evidence indicates that spectral variations in the present objects are produced by slope changes. We have showed as alternative explanations do not fit the data or do resort to "ad hoc" additional components, not supported by the observed spectral shape. Summarizing the observational picture, there are at least six Seyfert galaxies that show spectral variability above 1 keV, well described by variations of the spectral index of the continuum. In all these objects the spectrum becomes steeper when the (2–10 keV) luminosity is higher. The dynamics of spectral variations is also similar, corresponding to $\Delta\alpha \approx 0.3$–$0.4\ \Delta L/\langle L\rangle$, where $\langle L\rangle$ is the average X-ray luminosity. The spectral index changes are confirmed within the interval $\alpha \approx 1.4$–2, that is the same interval of values observed in different objects with luminosities ranging from less than 10^{41} to 10^{46} ergs s^{-1} (Mushotzky 1984; Petre *et al.* 1984; Reichert *et al.* 1985; Pounds 1985; Urry 1986). Finally, as appears from Figures 4 and 11, the spectra of MCG −6-30-15 and NGC 4051 corresponding to different intensity levels, have an intersection point around 30 keV, where the PHA ratio is one. If this spectral behavior extends at higher energies, we should expect an anticorrelation between the luminosity above 40 keV and the spectral index, the reverse of what observed in the LAC range.

What does this observational picture entail about the radiative mechanism of the X-ray continuum? First we note that the positive correlation between α and luminosity, when extrapolated over the five order of magnitude range of AGNs luminosities, falls well beyond the observed spectral index interval. In fact, this apparent disagreement implies that the spectral index is a function of luminosity *and* some other relevant parameter that balances the luminosities of different objects. For example, a key parameter appearing in many models (e.g., Lightman and Zdziarski 1987) is the compactness parameter $l_X = L_X \sigma_T/(R m_e c^3)$, where L_X is the 2–10 keV luminosity and R is the size of source. However, the distribution of α versus L_X obtained from the observations of several AGNs, does not show any evidence of correlation between the two quantities (see Fig. 11 of Lightman and Zdziarski 1987). This is not surprising, considering that the following effects can spread out this distribution: (1) other parameters, besides the compactness parameter, determine the spectral index. (2) The size of the source, R, is not well measured by the shortest time scale of variability. This effect could be particularly important in objects with power spectra as f^{-1}, as discussed by Lawrence *et al.* (1987). In fact, both MCG −6-30-15 and NGC 4051, that have this kind of power spectra, showed variability on time scale shorter than that observed in previous measurements by about one order of magnitude. The new l_X would be a factor of 10 greater than that used in Lightman and Zdziarski (1987). (3) Other objects, besides MCG −6-30-15, might be partially covered by a very thick screen absorbing the photons below 10 keV. As quoted previously, there are at least two other Seyfert galaxies that show a similar situation. In these objects, the observed 2–10 keV luminosity, L_X, would be only a fraction f_{cov} of the real luminosity, and the differences in f_{cov} among different objects would spread out the observed l_X distribution.

The observed positive correlation between the spectral index and luminosity provides strong constraints to radiative models and rules out those where the spectrum becomes harder when L_X increases, as Comptonization of seed photons by a hot electron gas with varying temperature (Guilbert, Fabian, and Ross 1982). A thorough discussion of this issue goes beyond the aim of this work. Here we just consider some implications on the pair production model of Lightman and Zdziarski (1987). They consider a spherical source in which a relativistic population of electron and seed photons is continuously injected. The output photon spectrum is computed in a stationary situation, taking into account Compton scattering of seed (and higher order) photons and electron-positron pairs produced by γ-γ process. The main parameters that define the spectral shape of the X-ray spectrum are the electron and seed photon compactness parameters and the shape of the electron distribution. Different relationships between α and l_X are obtained, according to the varying parameter, and, interestingly, in all these cases that α increases when l_X increases. On the other hand, only the spectra where the variations are driven by changes in the seed photon luminosity have an intersection energy around 30–50 keV, in agreement with that observed in MCG −6-30-15 and NGC 4051 (Derme 1989).

Finally we note that, with the exception of 3C 120, all the objects that show a correlation between α and L_X are low-luminosity active galaxies ($L_X < 3 \times 10^{43}$ ergs s^{-1}). This would be another important constraint for radiative models. However, a similar effect could also be explained by a selection effect against objects varying on a time scale greater than a typical X-ray observation (a few days), as high-luminosity AGN generally do (Barr and Mushotzky 1986).

The authors had critical discussions with K. Pounds, K. Nandra, and G. C. Stewart during the course of this work. We have pleasure in acknowledging their important contribution. The authors wish to thank G. C. Perola and N. Kawai for many advices on the paper, an anonymous referee for several useful suggestions and all the members of the *GINGA* team and launching staff of the Institute of Space and Astronautical Science for the support in data collection. L. P. wants to express his thanks to the Japan Society for the Promotion of Science for his fellowship. M. Y. thanks his Ph.D. adviser, M. Nakagawa.

REFERENCES

Antonucci, R. R. J., and Miller, J. S. 1985, *Ap. J.*, **297**, 621.
Arnaud, R. R. J., and Miller, J. S. 1985, *M.N.R.A.S.*, **217**, 105.
Barr, P., and Mushotzky, R. F. 1986, *Nature*, **320**, 421.
Basko, M. M. 1978, *Ap. J.*, **223**, 268.
Bevington, P. R. 1969, *Data Reduction and Error Analysis for the Physical Science* (New York: McGraw-Hill).
Branduardi-Raymont, G. 1986, in *The Physics of Accretion onto Compact Objects*, ed. K. O. Mason, M. G. Watson and N. E. White (Berlin: Springer-Verlag), p. 407.
Deeming, T. J. 1975, *Ap. Space Sci.*, **36**, 137.
Derme, C. D. 1989, in *Proc. 23rd ESLAB Symposium on Two Topics in X-Ray Astronomy*, ed. J. H. Hunt and B. Battrick (Noordwijck: ESA), ESA SP-296, p. 925.
Fabian, A. C., Rees, M. J., Stella, L., and White, N. E. 1989, *M.N.R.A.S.*, **238**, 729.
Ferland, G. J., and Rees, M. J. 1988, *Ap. J.*, **332**, 141.
Guilbert, P. W., Fabian, A. C., and Ross, R. R. 1982, *M.N.R.A.S.*, **199**, 763.
Guilbert, P. W., and Rees, M. J. 1988, *M.N.R.A.S.*, **233**, 475.
Halpern, J. P. 1984, *Ap. J.*, **281**, 90.
———. 1985, *Ap. J.*, **290**, 130.
Hayashida, K., *et al.* 1989, *Pub. Astr. Soc. Japan*, **41**, 373.
Holt, S. S., *et al.* 1980, *Ap. J. (Letters)*, **241**, L13.
Kallman, T. R., and McCray, R. 1982, *Ap. J. Suppl.*, **50**, 263.
Koyama, K., Inoue, H., Takano, S., Tanaka, Y., Ohashi, T., and Matsuoka, M. 1989, *Pub. Astr. Soc. Japan*, **41**, 731.
Krolik, J. H., and Kallman, T. T. 1984, *Ap. J.*, **286**, 366.
Kwan, J., and Krolik, J. H. 1981, *Ap. J.*, **250**, 478.
Lawrence, A., and Elvis, M. 1982, *Ap. J.*, **256**, 410.
Lawrence, A., Watson, M. G., Pounds, K. A., and Elvis, M. 1985, *M.N.R.A.S.*, **217**, 685.
———. 1987, *Nature*, **325**, 694.
Leahy, D. A., Matsuoka, M., Kawai, N., and Makino, F. 1989, *M.N.R.A.S.*, **236**, 603.
Lightman, A. P., and White, T. R. 1988, *Ap. J.*, **335**, 57.
Lightman, A. P., and Zdziarski, A. A. 1987, *Ap. J.*, **319**, 643.
Makino, F. 1987, *Ap. Letters Comm.*, **25**, 223.
Malkan, M. A. 1983, *Ap. J.*, **268**, 582.
Malkan, M. A., and Sargent, W. L. W. 1982, *Ap. J.*, **254**, 22.
Matsuoka, M., Ikegami, T., Inoue, H., and Koyama, K. 1986, *Pub. Astr. Soc. Japan*, **38**, 285.
Morrison, R., and McCammon, D. 1983, *Ap. J.*, **270**, 119.
Mushotzky, R. F. 1982, *Ap. J.*, **256**, 92.
———. 1984*a*, *Adv. Space. Res.*, **3**, Nos. 10–12, p. 157.
———. 1984*b*, in *X-Ray and UV Emission from Active Galactic Nuclei*, ed. W. Brinkmann and J. Trümper (Garching: Max Planck Institut), p. 108.
Nandra, K., Pounds, K. A., Fabian, A. C., and Rees, M. J. 1989, *M.N.R.A.S.*, 1236, 39p.
Pan, H. C., Stewart, G. C., and Pounds, K. A. 1988, in *Physics of Neutron Stars and Black Holes*, ed. Y. Tanaka (Tokyo: Universal Academy Press), p. 375.
Perola, G. C., *et al.* 1986, *Ap. J.*, **306**, 508.
Petre, R., Mushotzky, R. F., Krolik, J. H., and Holt, S. S. 1984, *Ap. J.*, **280**, 499.
Piro, L., Massaro, E., Perola, G. C., and Molteni, D. 1988, *Ap. J. (Letters)*, **325**, L25.
Piro, L., Yamauchi, M., and Matsuoka, M. 1990, *Ap. J. (Letters)*, in press.
Piro, L., Matsuoka, M., and Yamauchi, M. 1989, in *Proc. 23d ESLAB Symposium on Two Topics in X-Ray Astronomy*, ed. J. Hunt and B. Battrick (Noordwijk: ESA), ESA SP-296, p. 819.
Pounds, K. A. 1985, in *Proc. Japan–US Seminar on Galactic and Extragalactic X-Ray sources*, ed. Y. Tanaka and W. H. G. Lewin (Tokyo: ISAS), p. 261.
Pounds, K. A., and Turner, T. J. 1986 in *Variability of Galactic and Extragalactic X-ray Sources*, ed. A. Treves (Milano: Associazione Avanzamento Astronomia), p. 1.
Pounds, K. A., Turner, T. J., and Warwick, R. S. 1986, *M.N.R.A.S.*, **221**, 7P.
Pounds, K. A., Warwick, R. S., Culhane, J. L., and de Korte, P. 1986, *M.N.R.A.S.*, **218**, 685.
Reichert, G. A., Mushotzky, R. F., Petre, R. F., and Holt, S. S. 1985, *Ap. J.*, **296**, 69.
Reichert, G. A., Mushotzky, R. F., and Holt, S. S. 1986, *Ap. J.*, **303**, 87.
Rothschild, R. E., Mushotzky, R. F., Baity, W. A., Gruber, D. E., Matteson, J. L., and Peterson, L. E. 1983, *Ap. J.*, **269**, 423.
Rybicki, G. B., and Lightman, A. P. 1979, *Radiative Processes in Astrophysics* (New York: Wiley).
Shakura, N. I., and Sunyaev, R. A. 1973, *Astr. Ap.*, **24**, 337.
Turner, M., *et al.* 1989, *Pub. Astr. Soc. Japan*, **41**, 345.
Turner, T. J. 1987, *M.N.R.A.S.*, **226**, 9P.
Urry, C. M. 1986, in *Variability of Galactic and Extragalactic X-ray Sources*, ed. A. Treves (Milano: Associazione Avanzamento Astronomia), p. 15.
Wang, B., Inoue, H., Koyama, K., Tanaka, Y., Hirano, T., and Nagase, F. 1986, *Publ. Astr. Soc. Japan*, **38**, 685.
Warwick, R. S., Koyama, K., Inoue, K., Takano, S., Awaki, H., and Hoshi, R. 1989a, *Pub. Astr. Soc. Japan*, **41**, 739.
Warwick, R. S., Yaqoob, T., Pounds, K. A., Matsuoka, M., and Yamauchi, M. 1989b, *Pub. Astr. Soc. Japan*, **41**, 721.
White, T. R., Lightman, A. P., and Zdziarski, A. A. 1988, *Ap. J.*, **331**, 939.
Wilkes, B., and Elvis, M. 1987, *Ap. J.*, **323**, 243.
Yaqoob, T., and Warwick, R. S. 1989, in *Proc. 23d ESLAB Symposium on Two Topics in X-Ray Astronomy*, ed. J. Hunt and B. Battrick (Noordwijck: ESA), ESA SP-296, p. 1089.
Yaqoob, T., Warwick, R. S., and Pounds, K. A. 1989, *M.N.R.A.S.*, **236**, 153.

MASARU MATSUOKA and MAKOTO YAMAUCHI: Institute of Physical and Chemical Research, Wako-shi, Saitama, 351-01, Japan

TOSHIO MURAKAMI: Institute of Space and Astronautical Science, Yoshinodai, Sagamihara-shi, Kanagawa 229, Japan

LUIGI PIRO: Istituto Astrofisica Spaziale, C.N.R., C.P.67, 00044 Frascati (Rm), Italy